5 The Third Energy Transfer Process: Particle–Substrate Interactions

5.1 Basic Considerations

Coatings are built up particle by particle. The solidification time, t_{sol}, of a hot molten particle arriving at the cold substrate surface is orders of magnitude shorter than the intermission time, t_i, the time between the arrival of two particles flying in the same trajectory. Therefore, a particle does not encounter, on arrival, a permanent liquid melt pool as it would in welding processes. The cooling time from the freezing point down to ambient temperature is two to three orders of magnitude longer than the solidification time. This means that a limited degree of particle interaction by diffusion as well as some stress relief is still possible.

- The properties of the layered deposited material are determined by the:

- velocity and temperature of the particles on impact,
- relative movement of the plasmatron and the substrate, and
- substrate and coating cooling during spraying.

- The wetting and flow properties of the liquid droplets are of great importance. They influence the:

- coating porosity,
- morphology of the coating/substrate interface,
- cohesive bonding among splats and successive layers, and
- adhesive bonding to the substrate.

These influences will be discussed briefly in Sec. 5.5.

Flow and solidification of molten droplets on impact are difficult to treat theoretically because of interaction between heat transfer and crystal growth kinetics [1–4]. It is also necessary to take into consideration the propagation of shock waves into the flattened particles and the substrate. The study of particle splats on glass or ceramic slides ('wipe test') [5] is a useful method to determine quickly the degree of superheating and thus the viscosity of the liquid particle droplets (see Sec. 5.5.1).

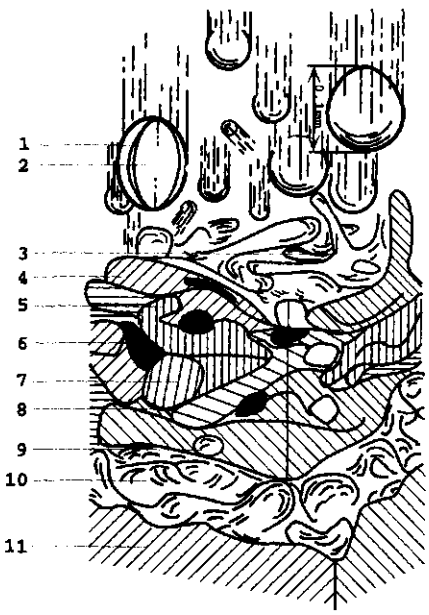

Figure 5-1. Schematic rendering of the chaotic structure of a plasma-sprayed coating layer 1: Thin molten shell; 2: unmelted core; 3: liquid splash; 4: 'pancake' splat; 5: interlocked splats; 6: oxidized particle; 7: unmelted particle; 8: pore; 9: void; 10: roughened substrate surface; 11: substrate [6].

Figure 5-1 shows an artistic rendering of the chaotic plasma spay process [6]. The molten droplets are thought to arrive one at a time, propagate along ballistic trajectories, and do not interfere with each other during flight ('ballistic model', see Sec. 5.5.1.3). A droplet with a diameter d_p impacts the solid substrate surface, and deforms to a so-called 'pancake' or 'Mexican hat' shape with a splat diameter D_s (Fig. 5-2). Entrained gases, unmelted and oxidized particles, and voids are mixed with the particle splats, and tend to degrade the coating properties because they provide points of stress concentration during in-service loading that will act as crack initiation centers. Particles with sizes substantially larger than the mean do not melt completely to their core and thus do not spread on impact. In their wake porosity can build up as well as trains of other only partially melted particles (Fig. 5-3). Thus it is extremely important to utilize spray powders with a narrow particle size distribution with a sufficiently small standard deviation.

5.2 Estimation of Particle Number Density

A quantitative estimation of the number of particles arriving at a defined surface area of the substrate in unit time, and the build-up of lamellae of the coating has been given by Houben [7] by considering spraying molybdenum powder (density $\rho_{Mo} = 10\,200\,kg\,m^{-3}$) of a mean particle size d_p of 50×10^{-6} m with a powder feed

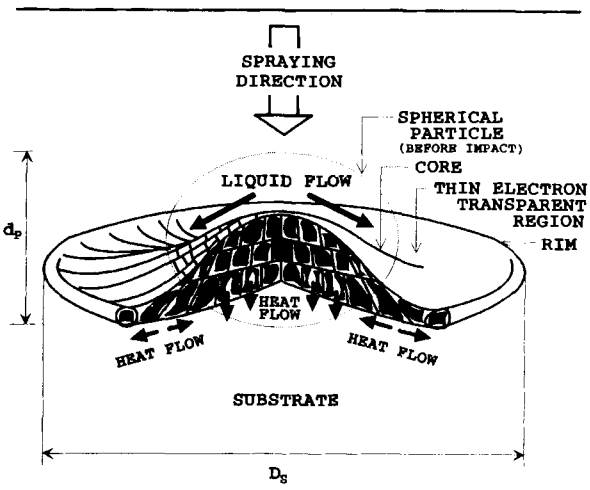

Figure 5-2. Deformation of a plasma-sprayed particle [6].

rate of $40\,\mathrm{g\,min^{-1}}$ ($6.7 \times 10^{-4}\,\mathrm{kg\,s^{-1}}$) onto a steel substrate. Thus, the number of particles injected into the plasma jet, N_1, is 10^6 particles per second[1].

The traverse speed of the plasmatron moving relative to the substrate is assumed to be $v = 4 \times 10^{-2}\,\mathrm{ms^{-1}}$, and the spray width, $w = 2.5 \times 10^{-2}\,\mathrm{m}$. The lamella diameter, D, of a single splat is $125 \times 10^{-6}\,\mathrm{m}$. With these parameters, the average number of lamellae on top of each other, N_2, after one pass of the plasmatron can be calculated with the assumption that all particles, N_1, injected will arrive at and stick to the substrate surface (deposition efficiency 100%) as follows.

The N_1 particles produce a total spray surface per unit time of

$$A_p = N_1(\pi/4)D^2 = 10^6[\mathrm{p\,s^{-1}}](\pi/4)(125 \times 10^{-6})^2[\mathrm{m^2}]$$
$$= 1.23 \times 10^{-2}\,\mathrm{m^2\,s^{-1}}. \tag{5-1}$$

Because the plasma jet moves, the covered substrate area will be

$$A_s = vw = 1.0 \times 10^{-3}\,\mathrm{m^2\,s^{-1}}. \tag{5-2}$$

Then the average number of lamelle on top of each other is

$$N_2 = A_p/A_s = 12. \tag{5-3}$$

The deposition time, i.e. the time required to lay down the N_2 lamellae, is $t_{dep} = w/v = 0.625\,\mathrm{s}$. The intensity of the bombardment of the surface is $n = N_1/w^2 =$

[1] Mass of single particle $m_p = V_p\rho_{Mo} = (4/3)\pi(d_p[\mathrm{m}]/2)^3\rho_{Mo}[\mathrm{kg\,m^{-3}}] = (\pi/6)(50 \times 10^{-6}[\mathrm{m}])^3 10.2 \times 10^3[\mathrm{kg\,m^3}] = 6.7 \times 10^{-10}\,\mathrm{kg}$. Powder feed rate $m = 6.7 \times 10^{-4}\,\mathrm{kg\,s^{-1}}$. Number of particles injected $N_1 = m/m_p = 10^6\,\mathrm{s^{-1}}$.

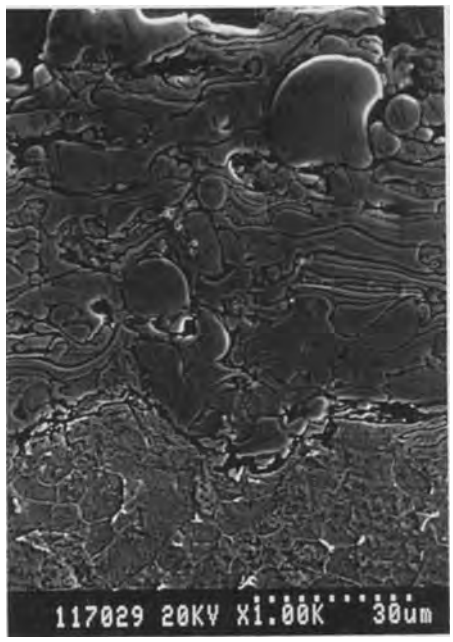

Figure 5-3. Development of porosity in the vicinity of large unmelted particles (85Fe15Si on low carbon steel, etched for 20 s in Nital).

1.6×10^9 particles per second per m^2. The surface receives per unit area $N_2 = t_{dep}n = N_1/vw = N_1/A_s = 1.0 \times 10^9$ particles m^{-2}.

Furthermore, the time elapsed between the arrival of two particles belonging to the ith and $(i+1)$th lamella plane is defined as t_i or 'intermission' time. It follows that:

$$t_i = w/vN_2 = 0.052\,\text{s}. \tag{5-4}$$

The solidification time for a 50 μm Mo droplet can be calculated using an approximate solution of the heat diffusion equation at the interface solid substrate/liquid droplet:

$$t_{sol} = x^2/4p^2a, \tag{5-5}$$

where x = lamella thickness, p = constant[2], and a = thermal diffusivity.

Numerically, for a lamella thickness of 7 μm,[3] the solidification time becomes $t_{sol} = (7 \times 10^{-6}[m^2])^2/4(0.582)^2(5.61 \times 10^{-5}[m^2\,s^{-1}]) = 6.5 \times 10^{-7}$ s.

---

[2] According to Houben [7], p is the Neumann–Schwartz parameter that can be estimated as the fitting parameter from the solidification time versus layer thickness relationship (Fig. 5-11).

[3] Assuming that the originally spherical droplet with a diameter $d = 50 \times 10^{-6}$ m and a volume V_p of 65.4×10^{-15} m^3 deforms on impact to a cylindrical disc of diameter $D = 125 \times 10^{-6}$ m of a volume $V_c = h(\pi/4)D^2 = 65.4 \times 10^{-15}$ m^3, the height h of the disc, i.e. the lamalla thickness is 5.3×10^{-6} m. Accounting for the 'Mexican hat' shape of the splat the geometric factor of 1.3 [4] transforms this value to an actual thickness of 7×10^{-6} m.

The ratio between intermission time and solidification time is $t_i/t_{sol} = 5.2 \times 10^{-2}[s]/6.5 \times 10^{-7}[s] = 80\,000$! This means that the time between two consecutive collisions is much longer than the time needed to solidify the droplets. Thus the liquid droplets are not likely to encounter a liquid surface, i.e. a weld pool does not exist. This is consistent with the view of plasma spray technology as a rapid solidification technology with cooling rates exceeding 10^6 to $10^7\,K\,s^{-1}$. It should be emphasized that Eq. (5-5) is only a very rough zero-order solution of the heat transfer (Fourier) equation. An exact solution is presented in Sec. 5.4.1, and a numerical example will be given in Sec. 5.4.2 and Appendix B.

With similar simple assumptions [7] further insight can be gained into the particle 'economy' and distribution at the substrate surface. Questions to be answered include how far two particles, on average, are apart, i.e. what their flight distance along a common trajectory might be. This distance, z_s, can be calculated simply by multiplying the intermission time, t_i, by the flight velocity, u_p, of the particles. If the flight velocity is $50\,m\,s^{-1}$, then with the time of $t_i = 0.052$ s calculated above, the flight distance between two particles becomes $z_s = u_p t_i = 50[m\,s^{-1}]0.052[s] = 2.60$ m.

On the other hand, the required flight distance between two particles in the same trajectory in order to meet a liquid preceding particle can not be longer than $z_l < u_p t_{sol} = 50[m\,s^{-1}]6.5 \times 10^{-7}[s] = 3.25 \times 10^{-5}$ m. Again, it is not likely that a particle will meet another liquid one.

While one particle solidifies at the surface, the number of particles arriving will be

$$N_3 = t_{sol} N_1 = 6.5 \times 10^{-7}[s]10^6[p\,s^{-1}] = 0.65 \text{ particles.} \tag{5-6}$$

These particles are distributed over the surface area $A_0 = (\pi/4)w^2 = 4.9 \times 10^{-4}\,m^2$. Thus the number of particles arriving per unit area during solification of one particle is

$$N_4 = N_3/A_0 = 0.65[p]/4.9 \times 10^{-4}[m^2] = 1326 \text{ particles}\,m^{-2}. \tag{5-7}$$

These N_4 particles will start to solidify simultaneously. Since they are very small but spread out over a large area, they will not interact with each other, i.e. the initial assumption of a ballistic deposition process is warranted. Experimental determination of the particle number density for model systems have been shown in Sec. 4.5.3.

5.3 Momentum Transfer from Particles to Substrate

Molten particle arrive with high velocities at the substrate surface, will be deformed, and as shown below, solidify partially due to the increase of the melting temperature with shock pressure. The flattening ratio D_s/d_p (D_s = splat diameter, d_p = original particle diameter; see Fig. 5-2) depends not only on intrinsic materials properties such as viscosity, μ, and density, ρ, of the liquid phase but also on the impact veloc-

ity, v_i, and the impact angle. A semiquantitative expression has been given by Madjeski [2] for a particle impact at an angle of 90° on a flat substrate as follows:

$$D_s/d_p = 1.3(\rho(v_i/\mu))^{0.2}. \tag{5-8}$$

Since the Reynolds number is given by $\mathrm{Re} = \rho v d/\mu$, an approximate relationship exists for the flattening ratio as

$$D_s/d_p \approx \mathrm{Re}^{0.2} \tag{5-8a}$$

assuming an isothermal particle [8]. However, due to the pronounced thermal gradients across the particles this relationship cannot be taken for granted in reality [9]. Also, the flattening ratio increases with increasing starting particle radius.

With deviation of the spray angle from 90° the properties of the coatings change depending on the nature of the sprayed material. For example, in case of molybdenum the cohesion within the coating increases by a factor of two for an angle of 45° whereas for alumina coating the cohesion increases slightly and the adhesion is uneffected. The deposition efficiency decreases for both materials with increasing deviation of the spray angle from 90° [10].

Recently several attempts were made to study theoretically the time-dependent deformation and solidification of molten droplets according to the Madejski model [11–13]. For example, Maruo *et al.* [11] solved the conservation law of mechanical energy using the *marker and cell method* [14]. As heat from the molten droplet is transported by the high speed flow of the spreading, cooling and solidification occurs at a much higher rate compared to the Madejski model that operates with the assumption of pure heat conduction. Also, a substrate with higher thermal conductivity results in a lower deformation ratio of the droplets. The work by Solonenko *et al.* [13] showed that for particle sizes of $d_p = 0.31$ mm the theoretical solution of the heat transfer equations scales satisfactorily with experimental results without taking into account any empirical constants under the conditions of a main regime parameters (MRP) control prior to impact. Those parameters were the velocity, temperature, size, density, thermal conductivity, and latent heat of melting of the particles, as well as the substrate temperature. One of the important results of the study was that the parameter

$$F_{p,s} = (\rho_{pm} L_p)/(\rho_{sm} L_s), \tag{5-8b}$$

where the subscripts p and s refer to particle and substrate, respectively, and m refers to the melting point, affects in a profound way the dynamics of simultaneous solidification and particle flattening. The parameter c_ξ (dimension: length) characterizes the thickness, h_s, of the molten layer of the substrate according to $h_s = c_\xi(\mathrm{Fo})^{1/2}$, and can be computed from the equation

$$c_\xi = F_{p,s}[c_\zeta + 2(q_2 - q_1)/\mathrm{Ku}_p], \tag{5-8c}$$

where q is the heat flux and $\mathrm{Ku} = L_p/c_{pm}T_{pm}$ is the Stefan–Kutateladze dimen-

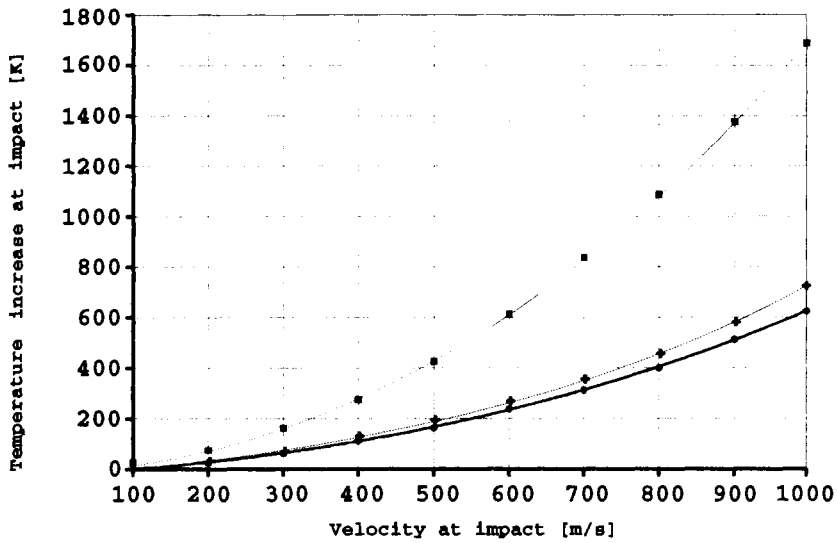

Figure 5-4. Dependence of the temperature increase due to particle impact on the particle velocity [16].

sionless group. If the heat flux into the melt, q_1, and into the substrate, q_2, are comparable than $F_{p,s} = c_\xi / c_\zeta$. The parameter c_ζ is a function of the Fourier number, Fo, and the Péclet number, Pe, and according to Eq. 5-8b it equals ρ_{sm}/L_s. It should be emphasized that the parameter $F_{p,s}$ is a criterion of the relative ease of melting (see Sec. 4.4.1). A second important finding of the study was that the theoretical as well as experimental results differ appreciably from those reported by Madejski [2] and Jones [15].

Particles traveling in a high velocity plasma as produced in a D-gun or under HVOF conditions acquire a high kinetic energy that on impact with a velocity v can be partially transformed adiabatically into heat according to

$$\Delta T = v^2/2c_p, \tag{5-9}$$

where c_p = specific heat at constant pressure. The temperature increase reaches appreciable values only for particle velocities exceeding about $400\,\mathrm{m\,s^{-1}}$ as shown in Fig. 5-4 [16]. The collision of particles with the substrate surface and with already deposited solidified particles, respectively, causes a deformation-induced melting within a thin surface layer thus generating a quasi-metallurgical bond at very high particle velocities [17]. Particle velocities of around $100\,\mathrm{m\,s^{-1}}$ lead to negligible temperature increase of only 5 °C on deceleration to zero speed assuming $c_p = 1000\,\mathrm{J\,kg^{-1}\,K^{-1}}$.

Apart from the transformation of kinetic impact energy to heat by an adiabatic process there is, however, another process that can lead to substantial particle and

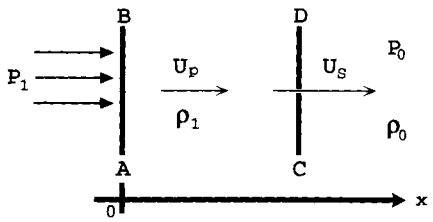

Figure 5-5. Shock wave front CD moving through a solid material (see text).

substrate heating by isentropic energy changes fascilitated by planar shock waves[4]. These shock waves obey the conservation equations of mass, momentum, and energy (Rankine–Hugoniot equation of state).

The shock wave concept can be illustrated by the idealized situation of Fig. 5-5. A uniform pressure, P_1, is suddenly applied to the thick slab of compressible material. This pressure is transmitted to the interior of the slab through a high-amplitude stress wave. If the material behaves normally in compression, i.e. if the compressibility decreases with increasing pressure, the wave front will essentially be a discontinuity in the stress and materials velocity fields, and in density and internal energy, and travels at supersonic speed with respect to the material ahead of the shock. This discontinuity is called a *shock wave*, characterized mathematically by a set of nonlinear hyperbolic differential equations. If P_1 remains time-invariant the state variables are constant between the boundary AB and the shock front CD. As shown in Fig. 5-5 the particle velocity is U_p and the shock wave front velocity is U_s. The mass flux density (in g cm^{-2} s^{-1}) into and out of the shock front is the product of the material density and the particle velocity relative to the shock front, $\rho_0(U_s - U_{p0})$ ahead of the shock and $\rho(U_s - U_p)$ behind the shock. Conservation of mass requires that

$$V/V_0 = \rho_0/\rho = (U_s - U_p)/(U_s - U_{p0}). \tag{5-10}$$

Momentum conservation is expressed through Newton's second law,

$$F = m(du/dt). \tag{5-11}$$

The force per unit area across the shock front is the pressure difference $P - P_0$, the mass flux per unit area is again $\rho_0(U_s - U_{p0})$, and the materials velocity change is $(U_p - U_{p0})$. Substituting into Eq. (5-11) the momentum conservation equation

$$P - P_0 = \rho_0(U_s - U_{p0})(U_p - U_{p0}) \tag{5-12}$$

results.

The conservation of energy across the shock front can be expressed by equating

[4] According to Trapaga and Szekely [8] the shock approach is not fully legitimate since the Mach numbers in normal plasma spray jets appear to be rather low (<0.05). However, with supersonic particle velocities obtained in D-gun or HVOF processes the assumption of shock waves are valid.

the work done per unit area and time by the pressure forces, $(PU_p - P_0U_{p0})$ to the sum of the kinetic energy change, $(1/2)\rho_0(U_s - U_{p0})(U_p^2 - U_{p0}^2)$ and the internal energy change $\rho_0(U_s - U_{p0})(E - E_0)$, i.e.

$$PU_p - P_0U_{p0} = (1/2)\rho_0(U_s - U_{p0})(U_p^2 - U_{p0}^2) + \rho_0(U_s - U_{p0})(E - E_0). \tag{5-13}$$

It can be shown [18] that combining Eq. (5-13) with Eqs. (5-10) and (5-12) yields the common form of the energy conservation equation

$$\Delta E = (E - E_0) = (1/2)(P + P_0)(V_0 - V), \tag{5-14}$$

where P and P_0 are the pressures behind and ahead of the shock front, and E and E_0 are the internal energies of the substrate material behind and ahead of the shock. The conservation equation in the form of Eq. (5-14) is called the Rankine–Hugoniot equation.

From the conditions of conservation of mass, momentum and energy, assuming $U_{p0} = 0$, it follows that

$$U_s/U_s - U_p = V_0/V, \tag{5-15a}$$

$$U_sU_p/V_0 = P - P_0. \tag{5-15b}$$

The conservation equations have intuitive geometric interpretations. Assuming $P_0 = 0$ in Eqs. (5-15a) and (5-15b), two definitions of the shock front velocity, U_s, and the particle velocity, U_p, can be derived as

$$U_s^2 = V_0^2/(P/V_0 - V) \tag{5-16a}$$

$$U_p^2 = P(V_0 - V). \tag{5-16b}$$

Any set of values for U_s and U_p correspond in the P–V diagram (Fig. 5-6) to a straight line $U_s = \text{constant}$ and a hyperbola $U_p = \text{constant}$. The intersection of the curves fixes the state of the shock compression with parameters P_1, V_1 in A through which the Hugoniot adiabatic P_H passes. The shock wave with a pressure P_1 results in a decrease of the specific volume $V_1 < V_0$. The pressure P_1 is composed of two contributions P_c and P_t. P_c is the 'cold' pressure resulting from the strong repulsive force of the interatomic potential, and P_t is the 'thermal' pressure associated with the thermal motion of atoms and electrons due to the shear compression. Therefore, as follows from Eq. (5-14), the total increase in internal energy (ΔE) is equal to the area of the triangle OAB in Fig. 5-6. This energy increment consists of an elastic component, ΔE_c (curvilinear triangle OCB) which is a result of the elastic (cold) pressure developing in the material, and a thermal energy component, ΔE_t, represented by the similar curvilinear triangle OAC. The shock transition provides both kinetic and internal energy to the material through which the shock wave propagates. Moreover, irreversible work is done on the material as it passes through the shock front. It can be shown that the entropy increases monotonically with pressure along the

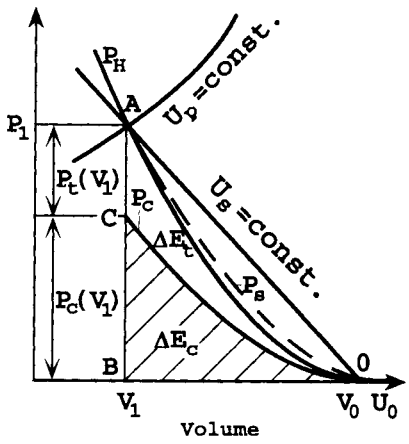

Figure 5-6. P–V diagram of the shock compression of a solid material. P_H is the Rankine–Hugoniot shock adiabat (see text).

Rankine–Hugoniot shock adiabatic that lies above the adiabatic passing though the initial state.

In as much as $\Delta E > \Delta E_c$, the shock–compression process is accompanied by heating of the substance and by an increase in its entropy which in turn leads to the appearance of the thermal pressure component P_t. It can be seen in Fig. 5-6 that the thermal energy and the thermal pressure increase progressively with increasing shock pressure. The shock temperature can be determined by the equation

$$T_A = T_C \exp[S_A/c_v], \tag{5-17}$$

where T_A = shock state temperature at state A (P_1, V_1) and T_C = adiabatic compression temperature at state C (P_c, V_1). On the other hand, during relaxation the heated material cools down, and the volume increases along the expansion isentrope P_s as shown by the dashed line in Fig. 5-6. The temperature after relaxation can be determined by

$$T_E = T_0 \exp[S_A/c_p], \tag{5-18}$$

where T_0 = temperature before the shock, and S_A = entropy in the shocked state.

The mechanics of a spherical molten particle with radius r colliding with the flat surface of a substrate at a velocity U_p can be approximated by Fig. 5-7. The inward moving shock front defines that portion of the material initially within the volume BOB that has been compressed into the volume BCB at time t. The contact face perimeter, a_t, moves outward with a velocity $\dot{a}_t$. It can be simply calculated by

$$a_t^2 = 2rU_p t - [U_p t]^2 \tag{5-19}$$

and the time derivative, i.e. the velocity at which the perimeter of the contact area moves outwards can be expressed as

$$da_t/dt = \dot{a}_t = U_p[r - U_p t]/[2rU_p t - (U_p t)^2]^{1/2} = U_p[r - U_p t]/a_t. \tag{5-20}$$

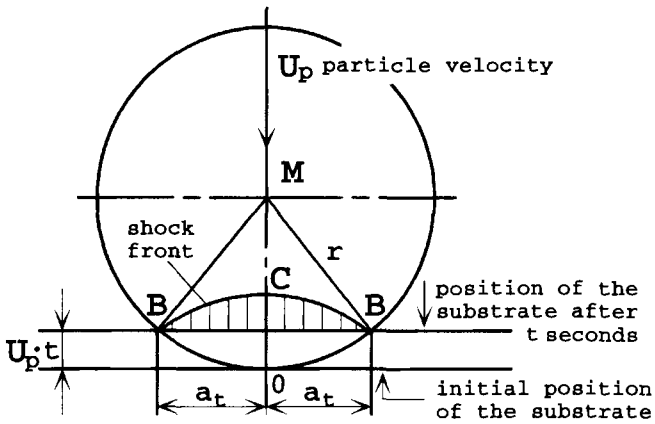

Figure 5-7. Collision of a spherical molten particle with a flat surface [7].

The following conclusions can be drawn [7].

1. The perimeter velocity $\mathring{a}_t$ increases with decreasing contact area radius a_t. For larger particles $\mathring{a}_t$ may even exceed the shock velocity, U_s.
2. The initial collision phase, arbitrarily defined by a contact area radius of 1 μm, lasts only 2×10^{-9} to 1.3×10^{-10} s for small (5 μm), and 5×10^{-10} to 3×10^{-11} s for larger (25 μm) particles.
3. The spreading velocity of the particles increases with size. The spreading process is about two orders of magnitude faster than the solidification time, t_{sol}.
4. During the process, adiabatic conditions prevail. Superheated particles will spread as a liquid from the start of the collision. This will provide good conditions for adherence of the coating to the substrate. Due to adiabatic shock heating the particle splats can spread more easily over the substrate surface. This improves adhesion by establishment of a thin diffusion layer, i.e. a metallurgical bond.

An important conclusion from the increase of the melting temperature of most substances with pressure (Clausius–Clapeyron's equation) is that a completely molten particle arriving at the substrate surface can partially solidify during collision not by conductive heat loss to the cold substrate but through adiabatic processes. This was used by Houben [7] to develop a tractable model to explain the occurrence of different types of splats (pancake-, flower-, and exploded-type). Figure 5-8 shows how the generation of a shock wave on particle impact modifies the spreading pattern of this particle. In the (subcritical) phase I ($t < t_c$) compression but no flow occurs. This situation corresponds to the one shown in Fig. 5-7. The shock front moves inward thus increasing the pressure and leading to partial solidification because of the pressure dependence of the melting temperature expressed by the Clausius–Clapeyron equation. In the post-critical phase II ($t > t_c$) the shock wave front squeezes out solid material laterally forming the typical flower pattern often observed in the 'wipe' test (see Sec. 5.5.1). In phase III the rarefaction wave accompanying the shock pressure

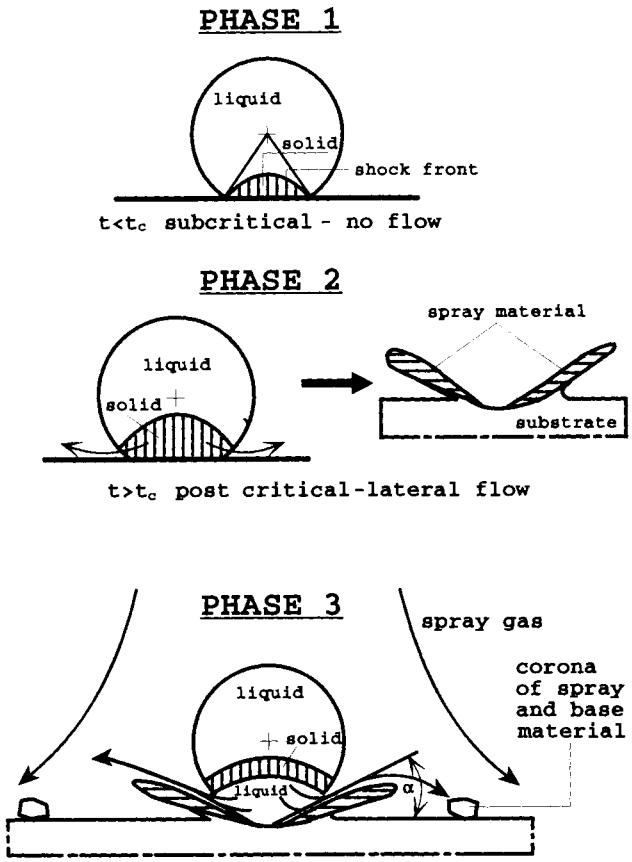

Figure 5-8. Spreading pattern of highly accelerated molten particles [7].

release moves in opposite direction towards the shock wave front. The compressed solid material of the droplet can relaxe and thus reliquify. This liquid materials now flows out sideways over the splat surface and forms a corona of spray material surrounding the splat. Depending on the critical radius of the outflow and the angle α, material tends to escape from the pressurized zone. The larger the critical radius the larger the potential energy stored in the pressurized zone. Instantaneous release of this pressure may lead to an explosive splat pattern that is detrimental to the coating cohesion as well as adhesion to the substrate.

Another type of pattern occurs during impact of highly superheated material presumably without the involvement of a partially solidified portion. Figure 5-9 shows frozen-in-time traces of superheated alumina splats with material ejected on impact through the shock process [19]. This ejected matter leaves behind voids that build up secondary microporosity in the plasma-sprayed layer. Very complex sequences of shock compression and rarefaction waves are being set up which generate non-equilibrium relaxation temperatures in 'hot spots'. These high local temperatures may delay solidification of the particle, and help to spread a liquid film across the surface of the substrate. In this way the adhesion of the coating to the substate can

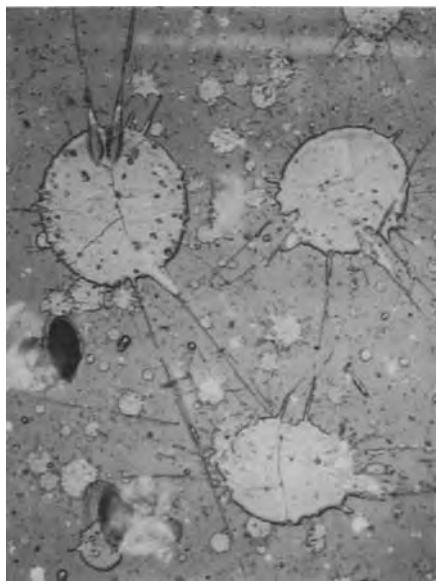

Figure 5-9. Frozen-in-time traces of superheated alumina splats with material ejected on impact [19].

be improved because the surface of the latter can melt partially to form a reaction boundary layer of intermediate composition [20].

Furthermore, the solidified part of an impacting particle on collision may undergo shattering by catastrophic fragmentation because of differential pressures across the particle. The leading face of the arriving particle is subjected to an average dynamic pressure

$$p_{\text{dyn}} \approx C_{\text{D}} \rho_{\text{p}} v^2/2, \tag{5-21}$$

with C_{D} = drag coefficient, ρ_{p} = plasma gas density and v = particle velocity. The pressure on the trailing face is much smaller. Integration of Eq. (5-21) over the surface of the spherical particle, $4\pi r^2$, yields the drag force

$$m\,(\mathrm{d}v/\mathrm{d}t) = -(1/2) C_{\text{D}} \rho_{\text{p}} A v^2 + (g/m) \sin \phi, \tag{5-22}$$

where m = particle mass, $A = \pi r^2$ = cross-sectional area, ϕ = angle between particle trajectory and plasma jet axis [21]. The second term in Eq. (5-22) can be neglected because of the short distance of travel of the particle. Fragmentation of the particle occurs when p_{dyn} in Eq. (5-21) exceeds the characteristic yield strength of the solid material.

5.4 Heat Transfer from Particles to Substrate

The Eq. (5-5) used above for the solidification time is only very approximate. It is the solution of the second-order differential equation of the thermal diffusivity (Fourier's

law) in exactly the same way that the expression $D = x^2/t$ is the approximate solution of the second-order differential equation of the chemical diffusivity (Fick's law).

Exact solutions require some mathematical 'inconveniences'. For the sake of completeness, and to show the elegance of the solution steps, the complete treatment will be given in Appendix B adopted from the work by Houben [7].

5.4.1 Generalized Heat Transfer Equation

The temperature at the substrate surface will be investigated by solving the heat transfer equations in a Cartesian coordinate system $[x, y, z]$. The temperature at the position x, y, z at the time t is $\Theta(x, y, z, t)$. The heat flux $\boldsymbol{j}$ per unit time and unit area is

$$\boldsymbol{j} = -a \operatorname{grad} \Theta, \tag{5-23}$$

and for the change of temperature with time follows

$$\partial\Theta/\partial t = -\operatorname{div} \boldsymbol{j}, \tag{5-24}$$

where a is the thermal diffusivity. Eliminating the flux $\boldsymbol{j}$ from Eqs. (5-23) and (5-24) by forming the divergence on both sides of Eq. (5-23), $\operatorname{div} \boldsymbol{j} = -a \operatorname{div} \operatorname{grad} \Theta$, and inserting this expression into Eq. (5-24), one obtains

$$\partial\Theta/\partial t = a\,\Delta\Theta \quad \text{or}$$
$$\Delta\Theta - (1/a)[\partial\Theta/\partial t] = 0, \tag{5-25}$$

where $\Delta \boldsymbol{a} = \operatorname{div} \operatorname{grad} \boldsymbol{a} = \partial^2\boldsymbol{a}/\partial x^2 + \partial^2\boldsymbol{a}/\partial y^2 + \partial^2\boldsymbol{a}/\partial z^2$ (Laplace operator).

Equation (5-25) is a partial differential equation of second order for the temperature Θ as a function of space and time. The starting condition is $\Theta(x, 0) = f(x) = \Theta_0 = T_{s0}$. The solution of Eq. (5-25) follows the Bernoulli method by anticipating $\Theta(x, t) = X(x)T(t)$ [22]. Introducing this assumption in Eq. (5-25) and dividing by XT, it follows that

$$X''/X - (1/a)[T'/T] = 0. \tag{5-26}$$

Equation (5-26) leads to two ordinary differential equations:

$$X''/X = k^2 \tag{5-27}$$

$$(1/a)[T'/T] = k^2, \tag{5-28}$$

where k^2 is a constant. The general solutions of those differential equations are

$$X = A_1 \exp(kx) + A_2 \exp(-kx) \tag{5-29a}$$

and

$$T = C_k \exp(ak^2 t). \tag{5-29b}$$

While there are no boundary conditions required for a one-dimensionally unlimited space, physically meaningful solutions must assure that the temperature Θ will not be infinite at $x = +\infty$ and $x = -\infty$. This would be fulfilled if Eq. (5-29a) did not contain an exponential function but only trigonometric functions. The term k^2 must therefore be negative, and consequently k must be imaginary. With $k^2 = -\kappa^2$, one obtains for the partial integral

$$(a_\kappa \exp(i\kappa x) + a_{-\kappa} \exp(-i\kappa x)) \exp(-\kappa^2 at). \tag{5-30}$$

From this expression a coefficient a_κ can be evaluated so that the starting condition $\Theta(x, 0) = \Theta_0$ is fulfilled:

$$a_\kappa = (1/2\pi) \int f(\xi \exp(-i\kappa\xi)\, d\xi. \tag{5-31}$$

Integration over κ, pulling out (at), and quadratic addition in the exponent of Eq. (5-30) eventually leads to

$$\begin{aligned}\Theta(x, t) &= (1/2(\pi at)^{1/2}) \int \delta(\xi - x_0) \exp(-[x - \xi]^2/4at)\, d\xi \\ &= (1/2(\pi at)^{1/2}) \exp[-x^2/4at],\end{aligned} \tag{5-32}$$

with $\delta(\xi - x_0) = \Theta(x, 0)$ (Dirac delta function). Full details of the derivation of Eq. (5-32) may be found in the literature [22].

From Eq. (5-32) the solution for the temperature profile of the substrate and the coating, respectively can be derived as

$$\Theta(x, t) = \Theta(x, 0) + \beta\{1 + \text{erf}[x/(4at)^{1/2}]\}, \tag{5-33}$$

where β = 'contact' thermal conductivity at the interfaces [7] and $\text{erf}[x/(4at)^{1/2}] = (1/(\pi at)^{1/2} \int \exp[-x^2/4at]$ (error function). These expressions will be used to calculate the temperature profile across a plasma-sprayed Mo coating on a steel substrate as shown in Sec. 5.4.2 and Appendix B.

5.4.2 Heat Transfer to Substrate

Figure 5-10 shows the coordinate system for the thermal diffusion from the particles into the substrate. The substrate surface is at $x = 0$, at $x = X(t)$ the interface between solid and liquid deposit. It will be assumed that for $x < 0$ the temperature approaches ambient conditions, i.e. $\Theta_0 = T_{s0}$ for $x \to -\infty$. The initial temperature condition of the particles in the plasma jet is $\Theta = T_3 > T_m$ for $x \gg 0$, where T_m is the

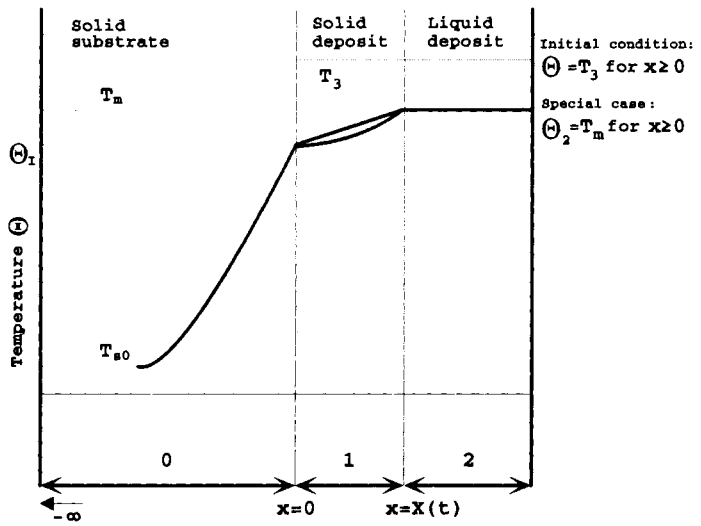

Figure 5-10. Coordinate system for solving the equations of heat transfer from the liquid/solid deposit into the substrate [7].

melting temperature of the particle. At the interface between liquid and solid deposit $\Theta = T_m$ for $x \geq 0$.

The heat transfer equations can be solved numerically with the following assumptions:

- heat transfer takes place only by conduction,
- thermophysical properties of materials are not temperature dependent,
- particle disks have uniform temperature (= melting temperature, T_m),
- supercooling or pressure dependent effects are absent in the contact area,
- melting of substrate does not take place[5].

Initial conditions are that the region $x > 0$ is liquid at the uniform temperature T_3, and the region $x < 0$ is solid at the uniform temperature T_{s0}. The treatment of the thermal diffusion (heat conduction) equations for the solid substrate (0), the interface substrate/solid deposit (1) and the interface solid deposit/liquid deposit (2) are given in Appendix B.

Table 5-1 summarizes the thermophysical quantities for Mo, low carbon steel and AISI-316 stainless steel [7].

The simplified solution of the thermal diffusion equations for the solidification time, $t_{sol} = x^2/4p^2a$ (Eq. (5-5)), are plotted in Fig. 5-11 against the thickness of the deposit of Mo and stainless steel AISI-316 on low carbon steel. Because of the much lower thermal conductivity of the stainless steel, the solidification time of a Mo droplet is considerably shorter than that of AISI-316 by t_{sol} (AISI-316)/ t_{sol}(Mo) = 7.55.

[5] As we will see later this requirement has to be relaxed for the deposition of a coating of a materials with an extremely high melting point (molybdenum) on a steel substrate.

Table 5-1. Numerical values of thermophysical quantities for iron, molybdenum and AISI-316 stainless steel used to calculate temperature profiles across the coating/substrate interface as well as contact temperatures [7].

Quantity	Fe	Mo	AISI-316	Unit
λ	75	146	18	$J\,s^{-1}\,m^{-1}\,K^{-1}$
ρ	7870	10200	7670	$kg\,m^{-3}$
$C = C_p$	460	255	489	$J\,kg^{-1}\,K^{-1}$
a	2.07×10^{-5}	5.61×10^{-5}	4.8×10^{-6}	$m^2\,s^{-1}$
T_m	1536	2610	1375–1400	°C
L	272×10^3	288×10^3	297×10^3	$J\,kg^{-1}$
$(\lambda\rho c)^{1/2}$	16478	19478	8217	$J\,m^{-2}\,K^{-1}\,s^{-1/2}$
$\frac{C(T_m - T_{s0})}{L(\pi)^{1/2}}$ [a]	1.4464	1.2938	1.2707	–
T_{s0}	20			°C
		Mo on Fe	AISI-316 on Fe	
B		1.1826	0.4987	–
$(B + \text{erf}\ p)pe^{p2}$		1.2938	1.2703	–
p		0.5487	0.6835	–
pe^{p2}		0.7415	1.0905	–
erf p		0.5622	0.6662	–
$(a_1/a_0)^{1/2}$		1.6463	0.4815	–

[a] e.g. for Fe: $\frac{C(T_m - T_{s0})}{L(\pi)^{1/2}} = \frac{460(1536 + 273 - 293)}{272 \times 10^3(\pi)^{1/2}} = 1.4464$

Figure 5-12 shows the temperature profiles across the interface solid Mo deposit/steel substrate (top) and solid AISI-316 deposit/steel substrate (bottom). The data points were calculated using the procedure shown in Appendix B for a thin AISI-316 layer (profiles 5 and 7) and a thick Mo layer (profiles 2 and 4). From Fig. 5-12 it can be seen that the contact temperature between Mo and steel of 1775.5 °C is high enough to melt a thin (1–2 μm) layer of substrate material thus likely improving adhesion because a solid solution of Mo in α-Fe can be assumed with a diffusion depth of approximately 20 nm [7].

5.5 Coating Diagnostics: Microstructure, Porosity, Adhesion, and Residual Stresses

5.5.1 Microstructure of Coatings

A few principles have to be considered that are important for assessment and control of the microstructure of ceramic coatings.

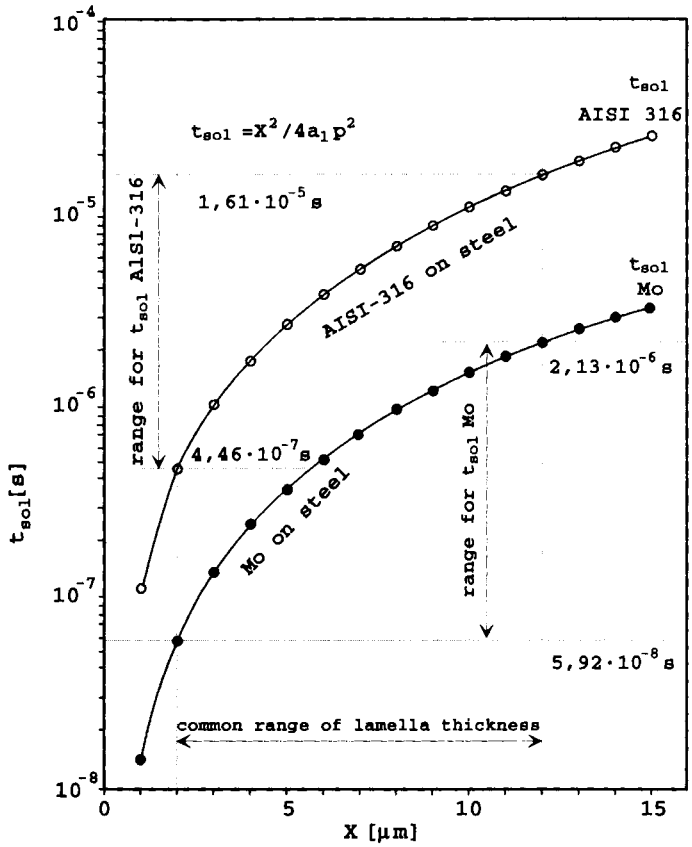

Figure 5-11. Solidification time of Mo particles, and AISI-316 stainless steel particles impacting on mild steel [7].

- Flow and solidification of the molten droplets upon impact is a very complex process.
- Solidification occurs in less than 1 μs.
- Complete cooling of an isolated particle of 50 μm diameter takes about 100 μs depending on the thermal conductivity of the material.
- The time between the arrival of two particles flying in the same trajectory is about 1 ms for a particle velocity of 100 m/s.
- Wetting and flow properties are very important.
- Coatings may possess fractal properties.

5.5.1.1 Splat Configuration

A rather good estimation of the flow characteristics of the molten particles can be obtained by applying the simple 'wipe' test [5]. A flat surface is quickly brought into the path of a molten particle trajectory with the intention of capturing only a

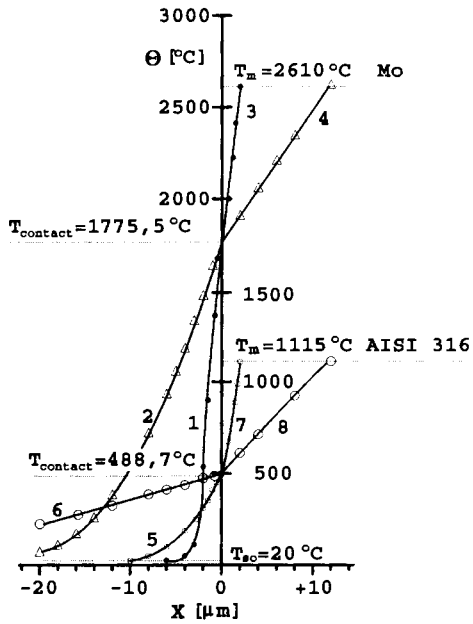

Figure 5-12. Calculated contact temperatures and temperature gradients at the interfaces Mo/mild steel and AISI-316/mild steel, respectively [7].

few particles. The solidified particle splats are investigated with optical or electron-microscopy. Figure 5-13 shows typical examples of hydroxyapatite particle splats obtained from an argon/hydrogen plasma jet under low-pressure conditions [23]. The plasma enthalpy, given here by the interaction of the plasma power and the stand-off distance, increases from Figs. 5-13a to 5-13d. In Fig. 5-13a (plasma power 45 kW, stand-off distance 26 mm) the enthalpy supplied to the particle is not sufficient to achieve melting. Figure 5-13b (plasma power 30 kW, stand-off distance 24 mm) shows a splat pattern of a particle whose outer rim has been melted but its core has remained highly viscous as exemplified by its porous microstructure. In Fig. 5-13c (plasma power 30 kW, stand-off distance 22 mm) a well-melted splat is shown whereas Fig. 5-13d shows the somewhat exploded splat (see Fig. 5-8) of a severely overheated particle (plasma power 45 kW, stand-off distance 22 mm).

Many modeling studies exist dealing with the behavior of particles impacting on a rigid substrate surface. Recently, Bertagnolli *et al.* [24] performed finite element calculations of the spreading process of ceramic liquid droplets on a flat cold surface and found that there is a correlation between the degree of flattening (Eq. (5-8)) and the initial process parameters. Since the mechanical performance of coatings depends crucially on the way particles flatten and establish intersplat bonding, such studies are very important to unravel the complex interaction of spray parameters and coating properties.

5.5.1.2 Surface Roughness of Coatings

Thermally sprayed coatings exhibit on mechanical treatment such as grinding, lapping and polishing very different surface structures compared with homogenous bulk

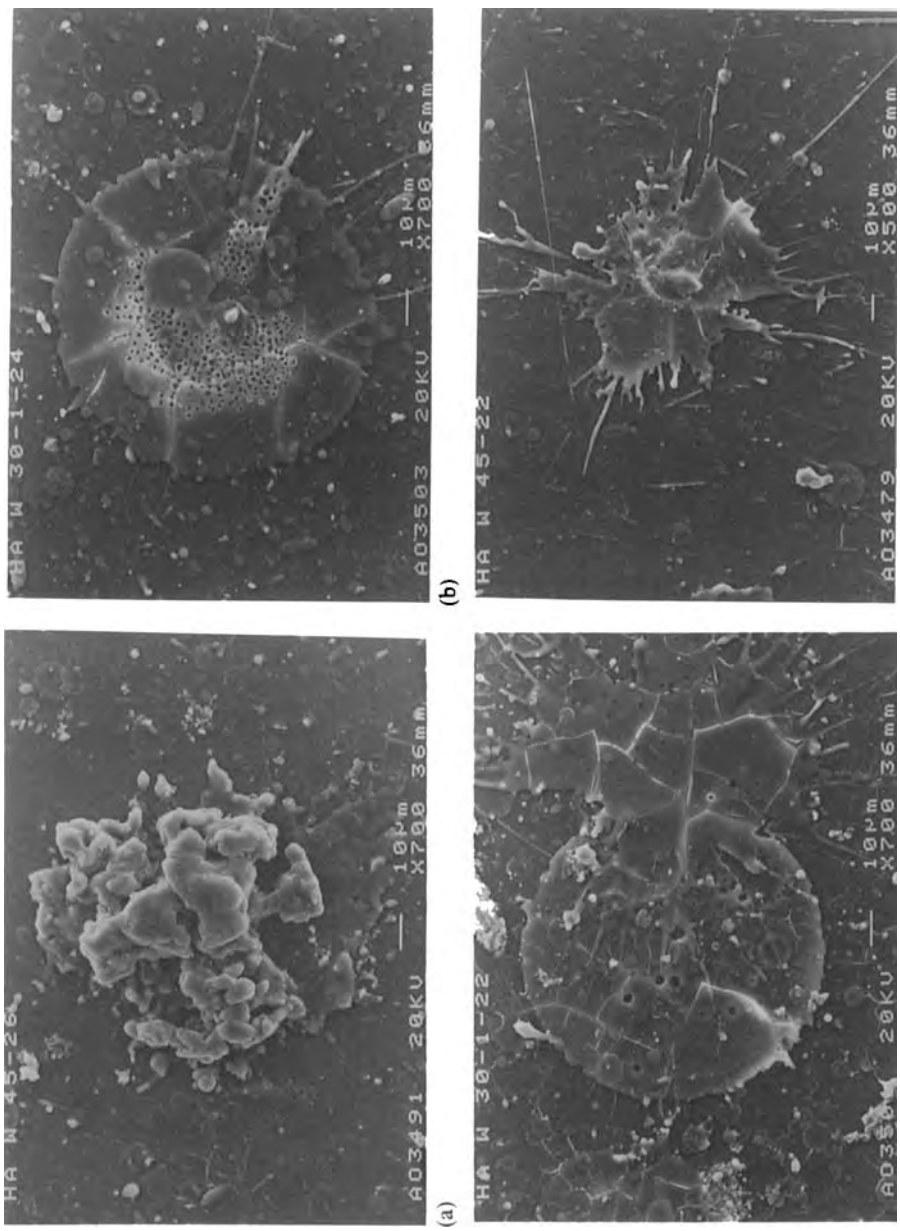

Figure 5-13. 'Wipe' test results on hydroxyapatite particles sprayed onto a glass slide (VPS argon plasma). For explanation see text [23].

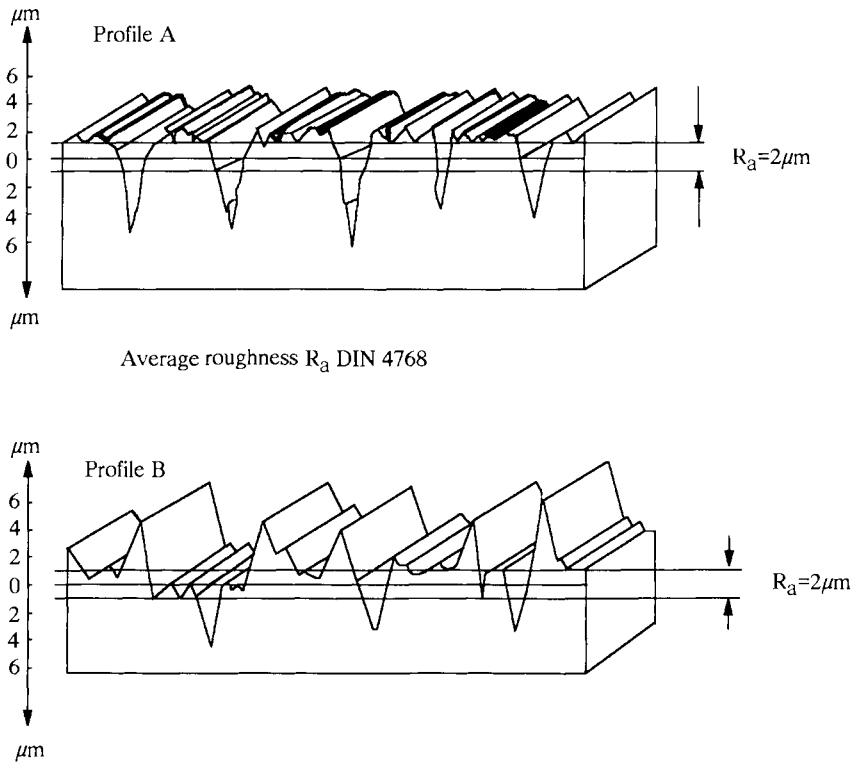

Figure 5-14. Surface roughness profiles of a plasma-sprayed coating. Despite identical average roughnesses two situations arise: a smooth plateau surface with depressions (profile A), and a strongly ragged surface with protrusions (profile B) [25].

materials. Homogeneous materials show after mechanical treatment a ploughed surface that is characterized by scratches; plasma-sprayed surfaces show an inhomogeneous profile given by the original splat structure, porosity and pulled-out and chipped-off areas. To describe such surfaces according to their functional behavior in service it is necessary to separate the undulation, i.e. the waviness of the surface (macroroughness) and the roughness *per se* (microroughness) that is responsible for the tribological behavior of the coating. Using a diamond-stylus surface roughness tester the profile obtained can be manipulated by electronic filtering methods so that a cut off-line is obtained that correspond to the long-wave surface profile [25]. Applying an RC high-pass filter (DIN 4768, ISO 3274) the information obtained from smooth surfaces with pores and pull-outs may be severely erroneous. This is shown in Fig. 5-14. The average roughness R_a (DIN 4768)[6] is measured to be

[6] The value R_a is the arithmetic mean of the deviation of the protrusions and depressions of the roughness profile from the average line, $R_a = (1/l\mathrm{m}) \int If(\mathrm{x})I\mathrm{dx}$.

identical for the two very different surface roughness profiles (smooth plateau surface with depressions, or strongly ragged surface with protruding asperities). Similar results are obtained for a comparison of the maximum roughness R_{max} and the median roughness R_z. Obviously, the first profile has a much larger 'carrying' surface, i.e. supports the countersurface of a bearing much more effectively than the second profile. The depressions of the first profile will also much more efficiently act as reservoirs for lubricating materials and thus promote the frictional properties of the coating. In order to describe the surface roughness more properly by determining the plateau-like amount of material, surface roughness should be measured by DIN 4776 [25]. Here the waviness of the surface can be determined by cutting-off the depressions, and application of digital phase-true filters to measure Abbot's curve of the amount of material 'carrying' the profile (Fig. 5-15). For thermally sprayed coatings the Abbot curve always has an S-shaped character. Approximating this curve by three straight lines the roughness profile can be subdivided into three areas: the core area of the profile, the spike area of the profile, and the depression area of the profile. The *reduced spike height* characterizes the height of the spikes protruding from the core area, the *reduced depression depth* characterizes the depth of the depressions below the core area.

5.5.1.3 Fractal Properties of Surfaces

Fractal geometry is a natural description for disordered objects ranging from macromolecules to the earth's surface [26]. These objects often display 'dilatation symmetry', meaning that they look geometrically self-similar under transformation of scale such as changing the magnification of a microscope. Many structures can be simply characterized by a single parameter D, the fractal dimension that is defined as the exponent that relates the mass M of an object to its size R [27]:

$$M \propto R^D. \tag{5-34}$$

This applies to Euclidian objects such as rods, discs, and spheres, for which the exponent D equals 1, 2, and 3 respectively consistent with the common notion of dimensionality (topological dimensions). However, for fractal objects the exponents need not be integral. While the objects described by Eq. (5-34) are called 'mass fractals' or polymers, 'surface fractals' are uniformly dense, i.e. colloidal, $D = 3$ as opposed to polymeric but have a rough surface. Such surface fractals share the self-similarity property[7] in the sense that if the surface is magnified, its geometric features do not change. Mathematically, surface self-similarity can be expressed analogously to Eq. (5-34) by

$$S \propto R^{D(S)}, \tag{5-35}$$

where S is the surface area and $D(S)$ is the surface fractal dimension. For a smooth object, $D(S) = 2$. For fractally rough surfaces, however, $D(S)$ varies between 2 and

[7] Note, however, that fractal sets are infinitely detailed but not necessarily self-similar.

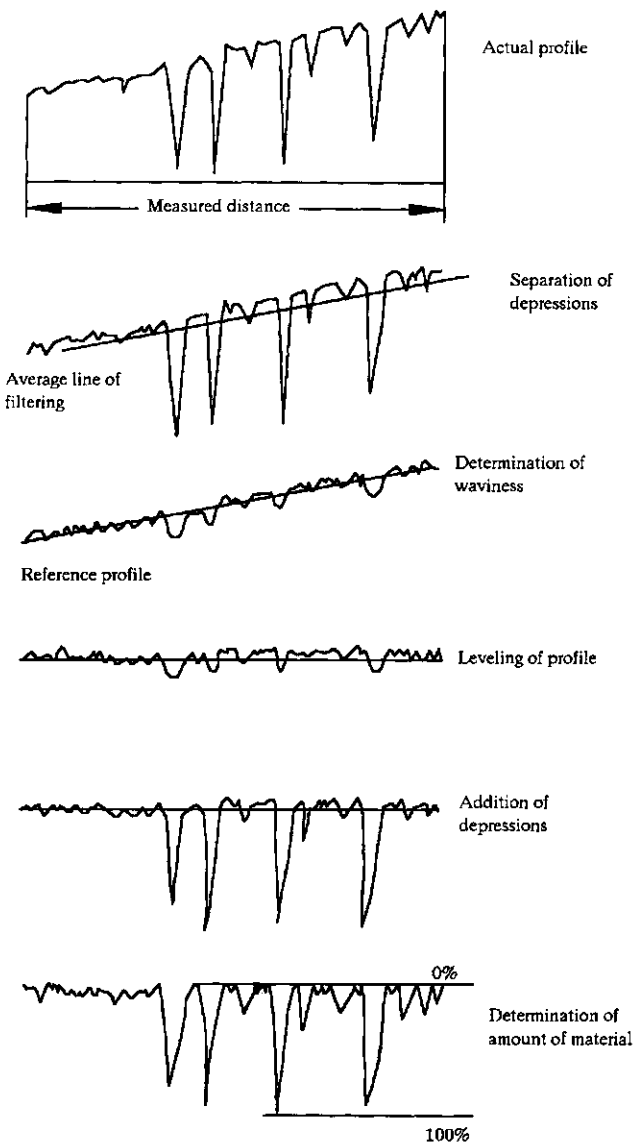

Figure 5-15. Determination of the waviness of a plasma-sprayed surface through Abbot's curve (see text) [25].

3, so that $D(S)$ is a measure of roughness [28, 29]. It should be emphasized here that fractals describe only the principle of ordering but do not give any information on the mechanism that leads to this ordering. A state-of-the-art treatise on fractals, in particular methods to determine fractal dimensions was provided recently by Stoyan and Stoyan [30].

A popular way to decribe the deposition of coatings is a ballistic model. In this

model particles are added, one at a time, to the growing deposit through randomly selected linear or ballistic trajectories [31]. In the most simple of these models the particles stick to the surface at the position at which contact is first made, i.e. surface diffusion is excluded. Also, since the conditions in the direction perpendicular to the surface are very different from those parallel to the surface, we will deal essentially with *self-affine geometries* [32]. Self-affine fractals are structures that can be rescaled by a transformation that involves a different change in length of scales in different directions. For example, whereas the scaling factor perpendicular to a plasma-coated surface may be on the order of micrometers, the scaling factor along the coated surface will be measured in millimeters or even centimeters. For structures of rough surfaces such as plasma-sprayed ones the approaches developed for self-similar structures are not strictly valid anymore and must be modified to account for this self-affinity. Since a rough surface can be represented by a single-valued function $h(\boldsymbol{x})$ of the position $\boldsymbol{x}$ in the lateral directions parallel to the surface, it is convenient to use the height difference correlation function $C_h(x)$ defined by

$$C_h(x) = \langle h(\boldsymbol{x}) - h(\boldsymbol{x}_0 + \boldsymbol{x}) \rangle_{|x|=x}. \tag{5-36}$$

to characterize the surface. It is reasonable to expect that the surface roughness $\xi_\perp$ will grow with some power of time according to

$$\xi_\perp \sim t^\beta, \tag{5-37}$$

assuming that the surface advances with a constant rate. The variance ξ^2, i.e. the amplitude of the waviness (see Sec. 5.5.1.3) is defined by $\xi^2 = \langle h_i - h^2 \rangle$ and is often used as a quantitative measure of the surface 'thickness' or roughness. For a growing fractal plasma-sprayed surface layer there will also be a characteristic correlation length $\xi_\parallel$ describing the lateral distance over which surface height fluctuations occur. This length is related to the former by

$$\xi_\perp \sim \xi_\parallel^\alpha, \tag{5-38}$$

and from Eqs. (5-37) and (5-38) it follows that

$$\xi_\parallel \sim t^{\beta/\alpha} \sim t^{1/z}. \tag{5-39}$$

Using these self-affinity scaling laws the height difference correlation function (Eq. (5-36)) can be expressed as

$$C_h(x, t) \sim t^\beta \mathrm{f}(x/t^{\beta/\alpha}). \tag{5-40}$$

The theoretical values of α and β are 1/2 and 1/3, respectively [33]. However, the true value of β may be obtained from the time dependence of the surface thickness (Eq. (5-37)). Numerical simulations of the dependence of the surface roughness (ξ) on the deposited layer thickness, h may be obtained from the literature [31].

It is quite tempting to apply the fractal approach to other plasma-sprayed coating properties. Fractal dimensions should provide information that may be used to de-

scribe not only surface roughness [34] but also surface area [28], fracture toughness [35, 36], adhesion strength [34], hardness, porosity, thermal conductivity and frictional properties of wear-resistant coatings. There are, however, to date but a few papers available in the literature that attempt to apply the concept of fractal geometry to describe coating properties even though the fractal approach will provide very fundamental answers to questions about the microstructure of thin surface coatings. For example, Yehoda and Messier [37] discussed the nature of very thin CVD layers in terms of a fractal structure. Their criterion was that fractal films should be self-similar at least over three orders of magnitude. This was not observed, however, but the development of pores in the film showed a scaling similar to the percolative scaling found by Voss *et al.* [38] in thin evaporated gold films.

Fractal dimensions can be determined from a variety of relationships that are unique to systems conforming to fractal geometries. Five of these relationships will be described in more detail below.

Box counting method

This method is the most simple way to evaluate fractal dimensions. The interface line of a surface roughness profile of a coating is shown in Fig. 5-16a. It is covered with boxes of side length d. If the interface line is completely covered with N squares than according to the rules of fractal geometry it holds that

$$N(d) = \mu d^{-D} \tag{5-36}$$

$$or \quad \log N(d) = -D \log d + \log \mu. \tag{5-37}$$

By continuously changing the size of the boxes d, i.e. the magnification scale, the number of squares $N(d)$ covering the interface line is counted. On plotting $\log N$ versus $\log d$ the slope $-D$ of the straight line obtained is the fractal dimension sought (Fig. 5-16b). Fractal geometry was used to investigate the dependence of the fractal dimension on the angle of grit blasting [34]. Even though the average roughness R_a did not change with blasting angle the fractal dimension was maximized at a blasting angle of 75° (Fig. 5-16c). This points to a more detailed rough surface with more undercuts and hook-like protrusions that will anchor a plasma-sprayed coating more strongly and thus improve coating adhesion by mechanical interlocking. The measurement and prediction of the fractal dimensions of grit-blasted surfaces will therefore be a very valuable tool to maximize coating adhesion. In particular, the R_a-values assessed normally will not give a true measure of the effective surface roughness as already pointed out in Sec. 5.5.1.2 but should be replaced by the fractal approach.

Density correlation function

The principle of this method is to find experimentally a density correlation function $C(r)$

$$\langle C(r) \rangle \propto r^{-\alpha}, \tag{5-38}$$

$$C(r) = (1/N) \sum \rho(r_i)\rho(r_i + r), \tag{5-39}$$

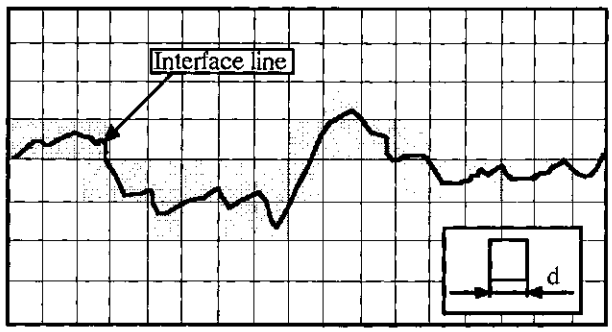

(a)

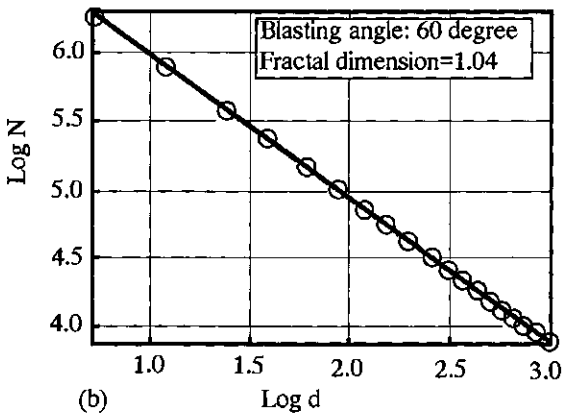

(b)

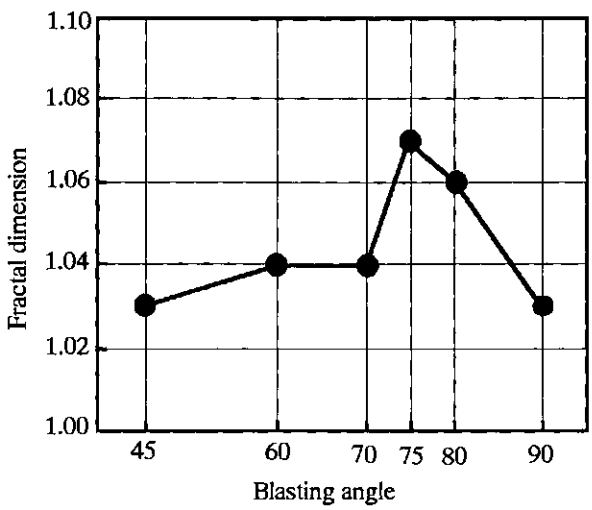

(c)

Figure 5-16. Box counting method to determine the fractal dimension of a plasma-sprayed coating [34].

where N is the number of splats, i is the observation point, $\rho(r_i)$ is the splat density at the observation point = 1, and $\rho(r_i + r)$ is the splat density at a point located a distance r from the observation point, and

$$-\alpha = D(\alpha) - d, \tag{5-40}$$

where $D(\alpha)$ is the fractal dimension, and d is the Euclidian dimension of the system [39]. In a 2D-section the density at the distance r is determined by the number of splats N divided by the area of a ring containing the N splats. For an inner ring of radius r and an outer ring of radius $(r + \Delta r)$ the density correlation function can be approximated by

$$\langle C(r) \rangle = \{N(r)\}/2\pi r \Delta r. \tag{5-41}$$

Plotting $\ln\langle C(r) \rangle$ versus $\ln(r)$ results in a straight line of slope $-\alpha$ from which the fractal dimension $D(\alpha)$ can be calculated according to Eq. (5-40).

Mass Correlation Function

This method is very similar to the preceding one. Fractal dimensions can be obtained from the relation

$$\langle M(r) \rangle \propto r^{D(\beta)}, \tag{5-42}$$

that may be obtained by integration of Eq. (5-41). M is the mass enclosed by some distance r. Assuming that each molten particle arriving at the substrate surface has equal mass, M can be replaced by the particle number $\langle N(r) \rangle$ contained within a sphere of radius r. Again, plotting $\ln\langle N(r) \rangle$ against $\ln(r)$ results in the slope $D(\beta)$. If $D(\alpha) \equiv D(\beta)$ than proof exists that the coating microstructure has fractal nature.

Slit island analysis (SIA)

This method is based on measuring the ratio perimeter/area of 'islands' that appear during successive removal of thin surface layers of a metal-coated fracture surface [40]. The surfaces obtained after each step are being investigated with modern image analysis software, and the perimeters P and areas F of newly appearing surface features recorded. Plotting of $\log P$ against $\log F$ of individual islands results in the slope $(D - 1)/2$ [36].

Fracture profile analysis (FPA)

Fracture profile analysis uses a Fourier analysis approach applied to a fracture surface to determine fractal dimensions [41]. Since the fracture profile can be considered a spectrum of microstructural information all signal-processing analytical tools developed for electric signals can be applied to fracture profiles. Many spectral details observed during analysis reflect the 'fundamental length', i.e. the correlation length (see above) of the microstructure and their related high-order harmonics. According to fractal hypothesis the integrated spectrum, i.e. the squared sum of the

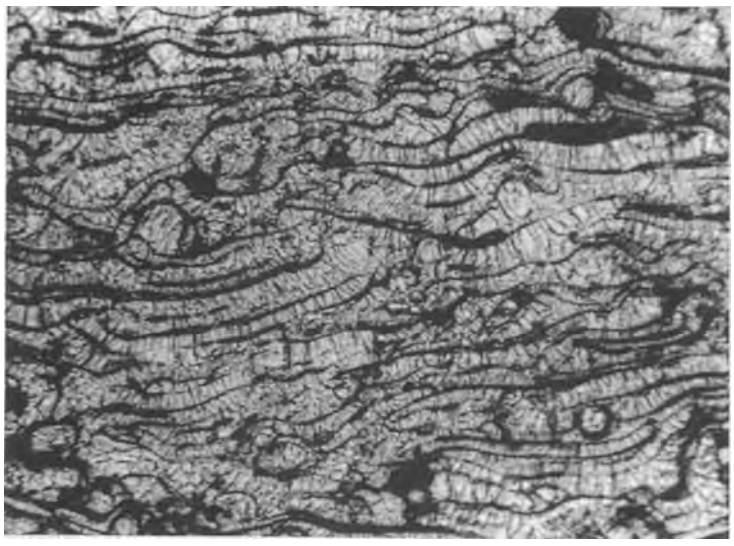

Figure 5-17. Microstructure of splats in an etched cross-section of a chromium coating on copper [66].

amplitudes takes the form $k^{-B'}$ where k is the wave number (inverse length) and $B' = B - 1 = 6 - 2D$ [36]. The fractal character of fractured coating surfaces can then be tested by plotting log(amplitude)^2 versus $\log k$ to obtain the slope B' from which the fractal dimension D can be calculated.

5.5.2 Porosity of Coatings

Whereas metallic coatings with nearly theoretical densities can be obtained by plasma spraying, the porosity of plasma-sprayed ceramic coatings is, in general, between 3 and 20%. While in some cases high porosity is advantageous, for example to reduce the thermal conductivity of thermal barrier coatings, to act as a retaining reservoir of lubricants in some wear-resistant coatings, or to enhance ingrowth of bone cells into bioceramic coatings, in most wear applications the wear resistance decreases dramatically with increasing porosity. Thus, porosity has to be tightly controlled in order to maximize coating performance.

Common causes of porosity are:

- shadow effects when splashing of a second particle over previously arrived ones may lead to a gap within one lamella layer (Fig. 5-3),
- narrow holes and/or gas inclusions between the ith and the $(i + 1)$th lamella (Fig. 5-17),

- inclusion of unmelted, larger particles (Fig. 5-3), and
- exploded particles due to overheating, excessive particle velocities and thus occurence of disruptive shock waves (Fig. 5-8, Fig. 5-13d).

Reduction of porosity includes the following measures:

- Preheating of substrate to increase the contact temperature and to reduce the viscosity of the impinging molten droplets.
- Use of low-pressure plasma spraying (LPPS) with increased particle velocities and thus increased kinetic impact energies.
- Post-spraying treatment such as
  - annealing of coatings to reduce microporosity by solid-state diffusion,
  - hot isostatic pressing (HIPping) of coatings [42],
  - laser surface densification [43–47], and
  - infiltration of coatings with polymers for low-temperature applications, Ni aluminides or other alloys for high-temperature uses [48], or by the sol–gel process [49].

Measurement of the porosity of plasma-sprayed coatings can be accomplished by a wide variety of methods that can be divided into those yielding as a result a simple number, the 'porosity' or pore volume related to the total volume of the coating in $cm^3\,g^{-1}$, and those that yield a pore size distribution function. In many cases the former methods are sufficient to characterize the porosity of a coating. The following methods can be applied.

- Point-counting using optical microscopy [50, 51].
- Electron-optical microscopy in conjunction with discriminant analysis of optical density using automated image analysis.
- Mercury pressure porosimetry using stepwise filling of smaller and smaller pore sizes with increasing pressure [52].
- Bubble pressure method using stepwise squeezing out of liquid from a completely filled pore ensemble [53].
- Dynamic penetration followed by measuring the electrical conductivity of the porous coating [54].
- Determination of the distribution function of pores by X-ray small angle scattering [55].

5.5.2.1 Point Counting

This approach is based on the quantitative relationships between measurements on the two-dimensional plane of polish and the magnitudes of the microstructural features in three-dimensional materials. The determination of the volume of pores is based on Gauss' principle that the spatial extention of a plane and a volume, respectively are determined by the number of hits that are obtained by randomly or regularly spatially distributed points in the various components of an aggregate. In modern point-counting techniques the points in space are points in a plane that are

counted optically or electronically. Thus the volume fraction occupied by a microstructural feature such as a void or pore, is equal to the point ratio of the selected feature as seen on random sections through the microstructure. Because point counting is tedious and special instruments for quantitative metallography are expensive, sometimes porosity is estimated by comparing the microstructures with standard photomicrographs. This methods is simpler, faster, and quite suitable for control and quality acceptance purposes. Depending on their purpose, comparisons are usually based on micrographs taken at magnifications ranging from 50 to 500 times [56].

5.5.2.2 Mercury Pressure Porosimetry

The technique requires fully automated equipment for pore size distribution functions ranging from 10 μm to 10 nm. It is based on the Washburn equation [57] that relates the diameter of a pore, r, to the pressure, p, required to fill it with a liquid. Since the ability of a liquid with a contact angle, ϕ, exceeding 90° to fill a pore is limited by its surface tension, σ, the applied pressure must overcome this surface tension:

$$r[\text{Å}] = 2\sigma \cos \phi / p, \tag{5-43}$$

where for mercury σ attains the value of 480 dyn cm^{-1} and $\phi = 140°$. The disadvantage of this method is that Eq. (5-43) is strictly valid only for cylindrical pores. For noncylindrical pores correction factors must be applied. This is particularly true for 'ink bottle' pores. Also, on application of high mercury pressures pore walls can be destroyed and higher porosities will be suggested.

5.5.2.3 Archimedes' Method

This is the classical method for determining the apparent density of a material and from this value the porosity. For plasma-sprayed metallic coatings a procedure has been suggested [58] involving the following steps:

1. Preparation of a solid cylindrical bar (12.7 × 2.2 cm).
2. Application of the coating approximately 2.8 mm thick for a length of about 6.4 cm.
3. Using the center holes, the bar is mounted on a lathe and the coated section is machined to a thickness of 2.54 mm.
4. Specimens of about 2.8 cm length are cut from both the coated and uncoated regions of the bar.
5. Both ends of the specimen are ground flat and perpendicular to the central axes.
6. Weighing of the specimens to an accuracy of 0.001 g.
7. Calculation of the volume.
8. Determination of the density of the coating using the following equation: (Weight of coated sample – weight of uncoated sample)/(Volume of coated sample – volume of uncoated sample). The volume fraction of porosity can be obtained

from 'measured' and 'true' density values by the equation: Pore volume fraction (%) = ('true' density – 'measured' density)/'true' density.

5.5.3 Adhesion of Coatings

Adhesion of coatings is controlled by three main mechanisms.

1. *Mechanical anchorage.* Surface roughness plays an overriding role. The particles must have sufficient plasticity, high impact velocity, low viscosity and good wettability. The adhesion strength of a ceramic coating is in many cases a linear function of the average surface roughness, R_a. However, as shown above the true influencing parameter appears to be the fractal dimension of the surface roughness.
2. *Physical adhesion.* This mechanism is controlled by diffusive bonding, where the diffusivity increases with increasing contact temperature according to Fick's law. This can be maximized by substrate preheating. Because of the small diffusion depth (produced by the rapid solidification), the diffusive adhesion generally plays only a minor role as an adhesion mechanism.
3. *Chemical adhesion.* Chemical adhesion can be engineered by adjusting the contact diffusivities. Thin reaction layers may be formed that improve the adhesion on a molecular scale by forming a true metallurgical bond.

In more detail, adhesion mechanisms can be classified as 'microbonding' and 'macrobonding' [59]. *Microbonding* refers to the bonding that takes place along very small surface areas the size of an individual particle of sprayed powder. *Macrobonding* refers to areas much larger by 10 to 100 times. Macrobonding relates to the macroroughness produced by threading and grooving methods or by extremely coarse grit blasting.

As indicated above, the microbonding between sprayed particles and the substrate, and between sprayed particles themselves, is never completely mechanical. There may be considerable bonding among particles at the microbond level, and no bond at all over a macroarea after a substantial coating has been built up. The reason for this is shrinkage. As each particle impinges at the substrate surface it flattens out, sticks to some extent, and then shrinks. An initial shrinkage occurs when the particle changes from a liquid, i.e. plastic to a solid, (rigid) state. In addition to this state-change shrink there is normal thermal shrinkage that continues as the particle cools down further. At the individual particle level shrinking may not cause much stress or at least not enough to rupture the microbond. A large body of evidence indicates a strong initial film adhesion between the sprayed particles and the substrate, and between neighboring particles. This microbonding mechanism is still not well understood. It is the same type of adhesion that occurs between an anodized coating and aluminum, or between chromium plate and steel. This adhesion has been variously referred to as 'film adhesion', 'solid-phase bond' or 'solid-state bond'. The bond may be very strong, nonmechanical, and occuring on a molecular level but is not usually referred to as 'metallurgical' or 'chemical bond'. Metallurgical bonds imply some alloying of the materials at the interface that normally is not observed in plasma-sprayed coatings. In the case of nickel aluminide coatings, however, the

exothermic reaction of this material causes alloying at the interface, and the result is a true metallurgical bond. Also, if very high contact temperatures occur at the interface as in the case of plasma-sprayed molybdenum on steel (see Sec. 5.4.2, Fig. 5-12), metallurgical bonding involving alloy formation is predominant.

Various test methods for evaluating coating cohesion and adhesion will be described in Chapter 7.

5.5.4 Chemical Changes

Frequently, the molten droplets react with the plasma gas, or with air pumped by the plasma jet. In particular, oxidation or decomposition of carbides and nitrides takes place. For example, a WC/Co coating may encounter three connected chemical processes:

1. matrix alloying, i.e. solubility of WC in the Co metal matrix under formation of so-called 'η-carbides' of the general composition Co_nW_mC,
2. decarburization, and
3. deoxidation [60].

The general equation for matrix alloying is

$$a\{WC\} + b\{Co\} + c\{O_2\} = d\{WC\} + e[Co_3W_3C] + f\{CO_2\} + \Delta H. \tag{5-44}$$

With increasing temperature and residence time in the hottest regions of the plasma jet decarburization reactions take place thought to occur in three stages [61, 62]:

$$2WC = W_2C + C \tag{5-45a}$$

$$W_2C + \tfrac{1}{2}O_2 = W_2(C,O) \tag{5-45b}$$

$$W_2(C,O) = 2W + CO \tag{5-45c}$$

As a consequence, HVOF spraying with lower temperature and shorter residence time considerably suppress tungsten and chromium carbide decomposition. Therefore, highly wear and corrosion-resistant coatings (see Sec. 6.1) are increasingly sprayed successfully with HVOF technique [63].

Figure 5-18 shows schematically the chemical and phase changes during thermal spraying of WC/Co(Ni) powder. It can be seen that the matrix of the coating consists in principle of an η-carbide with some residual WC, and a small degree of porosity [60].

A study by Brunet *et al.* [64] showed that during plasma spraying of TiC a severe carbon depletion occurs even when argon is used as a shroud gas to protect the

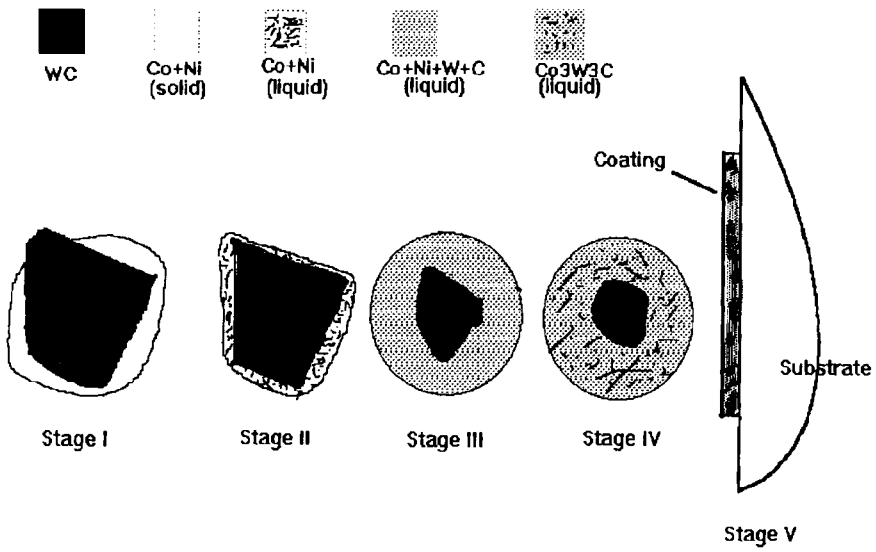

Figure 5-18. Schematics of chemical and phase changes during thermal spraying of WC/Co(Ni) powder [60].

sprayed TiC from oxidation. Plasma spraying in air results in the formation of crystalline oxides (Ti_3O_5, TiO_2) and free titanium [65].

5.5.5 Residual Stresses

The stresses occuring in the coating can be divided into microscopic, mesoscopic and macroscopic stresses.

Microscopic stresses are found inside individual splats, and are generated by the gradient of the coefficient of thermal expansion between the hot particle and the cooler substrate. Figure 5-17 shows the etched cross-section of an RF inductively-sprayed chromium coating with stress-induced cracks in the individual particle splats perpendicular to the splat boundaries [66].

Mesoscopic stresses occur between particle splats inside a lamella, and are responsible for reduced coating cohesion. They result principally from frozen-in contraction of the rapidly quenched molten particles at the substrate interface (see below).

Macroscopic stresses occur between the coating as a whole and the substrate. They depend on the temperature gradients within the coating between passes of the torch which decrease when both the thickness of the lamella and the spray width are being decreased. Macroscopic stresses can be controlled by

- cooling with gas jets: compressed air or carbon dioxide [67],
- cooling with liquid gases such as argon or carbon dioxide,

- adjustment of the relative velocities of torch/substrate, or
- grooving of substrate.

Since residual coating stresses influence the quality and the service life of coatings, in particular their adhesion and wear performance, it is the goal of any coating development to minimize such stresses. The origin of residual stresses is twofold. First, rapid quenching of the molten particles at the substrate interface results in frozen-in particle contraction, and tensile forces between individual particles add up to residual stresses states of the first order ('macro' residual stresses) throughout the coating [68]. Second, the differing coefficients of thermal expansion of coating and substrate contribute to the total stress state of the system. If this stress state exceeds the adhesive or cohesive bonding forces of the coating crack formation or delamination occur [69]. Stresses at the coating/substrate interface can be determined approximately by the Dietzel equation [70, 71] that uses the differences in the coefficients of thermal expansion of coating and substrate, the temperature gradient, and the thickness ratio to calculate the coating stress:

$$\sigma_c = \{E_c(\alpha_c - \alpha_s)\Delta T\}/(1 - \nu_c) + [(1 - \nu_s)/E_s]\, d_c/d_s\}, \tag{5-46}$$

where α is the linear coefficient of thermal expansion, ν is the Poisson ratio, E is the modulus of elasticity, and d is the thickness. The subscripts c and s refer to coating and substrate, respectively. For $\alpha_c > \alpha_s$ compressive stresses develop in the coating and tensile ones in the substrate that can be minimized by maximizing the ratio d_s/d_s. Thus for given values of ν and E the coating stresses increase with increasing coating thickness (compare Fig. 5-20b).

Residual tensile stresses are particularly severe in ceramic–metal composite coatings because of the generally large difference in the coefficients of thermal expansion of ceramic and metal. Their states can be determined, in principle, by borehole (blind hole), and X-ray or neutron diffraction measurements.

5.5.5.1 Blind Hole Test

A hole is drilled into the coating and the measurement of the relaxation occuring allows estimation of the original stress state [72]. A strain gauge based either on a semiconductor circuit or a modified Wheatstone bridge and glued to the coating surface is employed to record the relaxation. The measuring principle is based on the expansion-resistance effect of metallic conductors according to Wheatstone and Thomson. The change of the resistance of a conductor subjected to tensile or compressive forces can be attributed to the deformation of the conductor as well as to the change of its specific resistance due to changes of the microstructure. The relaxation of the coating material on drilling of a borehole results in an expansion or contraction of a measuring grid of strain gauges that in turn is recorded as a change in resistance[8]. Since this method is affected in various ways by external parameters it

[8] Actually the released surface strain measured with the strain gage rosette is converted to stress using a calibration curve and Hooke's law [75].

can only be used as a qualitative or at best semi-quantitative indicator of the stress state. Thus it has been suggested to use this method concurrently with other techniques such as X-ray diffraction measurement [73]. A more quantitative treatment of the method can be found by Bialucki *et al.* [74].

5.5.5.2 X-ray Diffraction Measurements ($\sin^2 \psi$-Technique)

The determination of the stress state is based on the measurement of the lattice deformation of a polycrystalline materials subjected to stresses. This is accomplished by measuring the change of the D-values of the interplanar spacings of selected lattice planes $\{hkl\}$ relative to the stress-free state, D_0:

$$\mathrm{d}D = D - D_0. \tag{5-47}$$

Since the penetration of the radiation into the coating is quite limited (1–10 μm) only the stress state of the coating surface can be measured. To obtain a stress distribution profile the surfaces must be consecutively removed by polishing, sputtering or etching, and the measurement be repeated.

Differentiation of the Bragg equation $n\lambda = 2D \sin \theta$ yields the (relative) lattice deformation

$$\varepsilon^{\mathrm{L}} = \mathrm{d}D/D_0 = -\cot \theta_0 \, \mathrm{d}\theta. \tag{5-48}$$

From Eq. (5-48) it follows that the change of the Bragg angle, $\mathrm{d}\theta$ is maximized for a given ε^{L} when θ_0 is large. Therefore, interplanar spacings with the largest possible Bragg angles must be chosen. Also, $\mathrm{d}\theta$ increases with increasing stress, σ, and decreasing Young's modulus, E. However, ceramic materials generally have large E values. Therefore, very small shifts of the interplanar spacings must be recorded with high accuracy. This requires highly sophisticated X-ray diffraction hardware and appropriate software [76].

Figure 5-19a shows the sample-based coordinate system used to deduce the basic equations for stress measurements. The lattice deformations $\varepsilon^{\mathrm{L}}_{\phi,\psi}$ measured close to the surface obtained according to Eq. (5-48) in the directions ϕ, ψ are taken as the deformations $\varepsilon_{\phi,\psi}$ expected from the theory of elasticity. The angle ϕ is the azimuthal angle to the x-axis, and the angle ψ is the distance angle to the z-axis, i.e. the surface normal N of the sample. For a triaxial stress state $\{\sigma_1, \sigma_2, \sigma_3\}$ with σ_1 and σ_2 parallel to the surface the distribution of the deformation is given by

$$\begin{aligned} \varepsilon_{\phi,\psi} = {} & \{(1+\nu)/E\}[\sigma_1 \cos^2 \phi + \sigma_2 \sin^2 \phi - \sigma_3] \sin^2 \psi \\ & -(\nu/E)[\sigma_1 + \sigma_2] + \sigma_3/E, \end{aligned} \tag{5-49}$$

where ν = the Poisson ratio and E = Young's modulus. Owing to the uniaxial stress state of ceramic coatings [77], $\sigma_3 = 0$. With this the general equation for determination of the stress state is obtained as

$$\varepsilon_{\phi,\psi} = (s_2/2)\sigma_\phi \sin^2 \psi + s_1(\sigma_1 + \sigma_2), \tag{5-50}$$

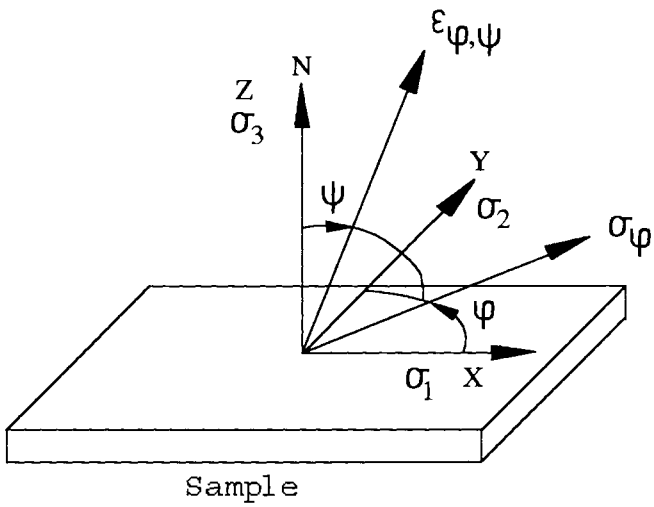

(a)

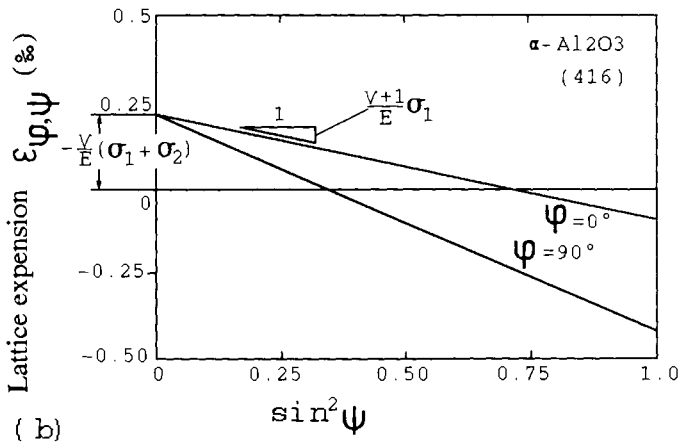

(b)

Figure 5-19. (a) Sample-based coordinate system for residual stress measurements, (b) lattice expansion against $\sin^2\psi$ for (416) of alumina [76].

with $\sigma_1 \cos^2\phi + \sigma_2 \sin^2\phi = \sigma_\phi$ (see Fig. 5-19a) and $s_1 = -\nu/E$, $s_2/2 = (1+\nu)/E$. Figure 5-19b shows an example of a plot of $\varepsilon_{\phi,\psi}$ versus $\sin^2\psi$ for the interplanar spacing (416) of alumina. From the slope of the lines the surface stress component σ_ϕ, and from the intersection with the ordinate axis ($\varepsilon_{\phi,\psi=0}$) the sum of the main stresses ($\sigma_1 = -100\,\mathrm{N\,mm^{-2}}$, $\sigma_2 = -200\,\mathrm{N\,mm^{-2}}$) can be obtained [76]. Figure 5-20a explains the often observed dependency of the residual stresses on the stand-off distance for a APS Al_2O_3/2.5% TiO_2 coating on St 37 steel using an NiAl bond

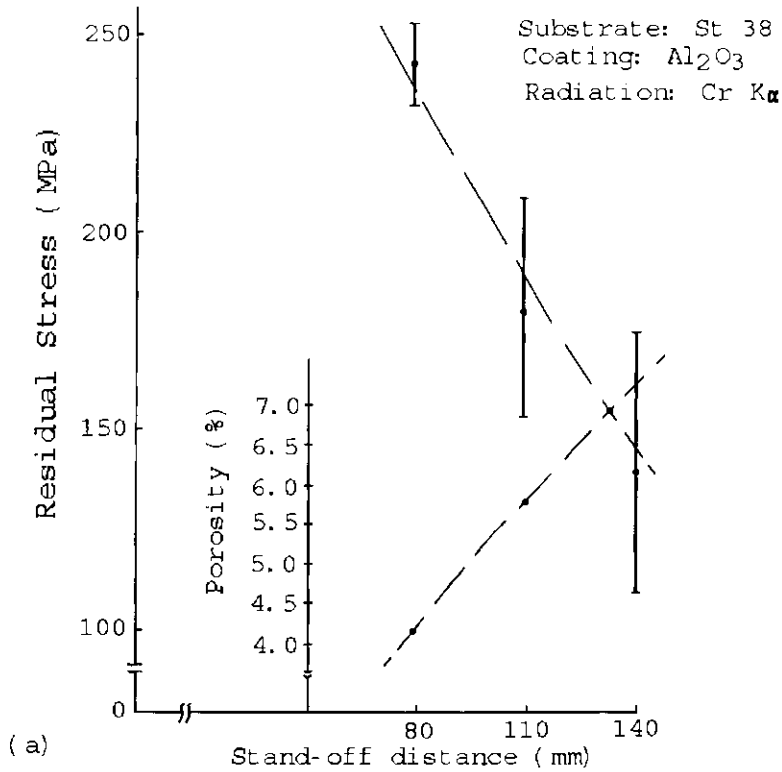

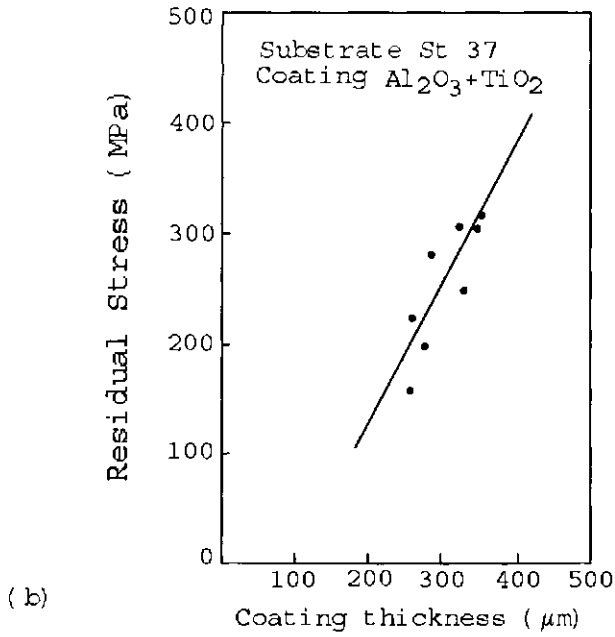

Figure 5-20. Dependence of the residual stress of an Al_2O_3/2.5% TiO_2 coating on St 37 steel on (a) the stand-off distance and (b) the coating thickness [77].

coat [77]. As the stand-off distance increases the increasing coating porosity may cause the material to attain a quasi-elastic behavior that can compensate for differences in the coefficients of thermal expansion of the coating and the steel substrate. This has been confirmed by Berndt [78] who suggested that plasma-sprayed coatings have a high compliance since the bonding force between lamellae is low enough to permit some relative sliding. In Fig. 5-20b the linear increase of the residual coating stresses with the coating thickness is shown (see also Eq. (5-46)). It should be emphasized that the results shown in Fig. 5-20 do not consider the possibly different contributions of the alumina and the titania phases to the total stress pattern. Such different stress responses have been demonstrated for t-ZrO_2/α-Al_2O_3 [76] and (Ti, Mo)C/NiCo [79] coatings. In particular, the former example has shown that a stress equilibrium exists between individual ceramic phases that can be described by a simple additive mixing rule [76].

A major problem exists in unequivocally describing the surface stress states by X-ray diffraction measurements. Since the deformation, ε, is dependent on material parameters such as the Poisson ratio, ν, and the modulus of elasticity, E, (see Eq. (5-38)), those quantities must be known with rather high accuracy. However, the bulk modulus of elasticity is certainly different from that of a coating owing, in particular, to the increased porosity of the latter [73]. Furthermore, free standing coatings have to be used to determine experimentally the value of E. This means that for every coating system the dependency of E on the porosity must be determined in-parallel to the determination of the stress state for each plasma spray parameter set. As a consequence the method becomes extremely time-consuming and cannot be applied routinely in industrial practice. Also, the continuous removal of surface layers changes the stress state, and the surface roughness established by cutting or lapping may lead to scattering of the X-rays and thus to line broadening that influences the accuracy of the measurement. Furthermore, since the modulus of elasticity, E, is a sensitive function of the stresses present in the coating[9] but the coating stress is attempted to be calculated using E as a determining parameter, conditions of nonlinearity exist.

Another factor affecting the evaluation of the $\sin^2 \psi$-plots is the often observed fact that severe internal residual stresses can result in a deviation from the true crystal symmetry. In titanium nitride [80] or hafnium nitride [81] coatings stresses in the coating plane cause densification and account for the distortion from cubic symmetry as evidenced in Nelson–Riley extrapolation function plots [80, 82].

5.5.5.3 Almen-type Test

To circumvent the drawbacks of the $\sin^2 \psi$-technique described above including the problem of a nonlinear modulus of elasticity, attempts have been made to apply other tests to get an estimate of the residual stresses. The so-called Almen test for

[9] The modulus at low stress levels or under conditions of the existence of a complex tension/compression stress pattern [84] is greater than that existing at pure tension and plastic flow of the material [78].

determination of the efficacy of shot peening applied to induce compressive stresses at the surface of metallic workpieces has been adapted to thermally sprayed thin coatings [68]. A thin test strip is mounted on a holder [83] and blasted with shot. This treatment leads to curving after removal from the fixture. The peened side of the curved strip will be convex. The degree of curving, measured with an appropriate gage, is a function of the residual compressive stresses developed in the strip. For estimation of residual stresses in thermally sprayed coatings a thin foil of the substrate material will be clamped to the Almen fixture and treated exactly in the same way as the substrate to be sprayed, i.e. grit blasting, ultrasonically cleaning, and spraying. After each working step the strip is being removed from the fixture and its stress state as displayed by the degree and direction of its curvature is determined. Fig. 5-21a shows the mounting block for the Almen test [83], Fig. 5-21b shows the thin foil before and after grit blasting. The induction of compressive stresses led to a convex curvature of the grit-blasted side of the foil that was reduced by the amount of the tensile stresses induced during coating. The reduction of the arc height, in this example 0.20 mm, can be directly related to the tensile residual stress state in the coating [63, 68].

5.5.5.4 Theoretical Analysis of Residual Stresses

Because of the complexity in terms of error possibilities, time and cost requirements of the X-ray diffraction-based measurements attempts have been made to solve the stress state determination in coatings by mathematical means. The mathematical models applied are subsequently validated by experiments. Thus the influence of individual parameters on the residual thermal stress state of the coatings can be studied, and the in-service behavior of the coating/substrate system predicted [85].

A model developed by Knotek *et al.* [86] is based on compartmentalization of the coating deposition process into time increments of 10^{-6} s. The coating thickness will be calculated for each time element and also the temperature distribution for the entire coating/substrate tandem from the difference of the amounts of heat introduced and dissipated. The thermal constraints are the convective heat losses at the surfaces, ideal contact between substrate and coating, and negligible radiation losses. Then the internal thermal strain state can be described by a two-stage model as follows.

In the first stage the total lateral expansion of the plate-shaped coated workpiece is found by numerical integration of the equation

$$\partial^2 x_i/\partial t^2 \sum m_i = x_i \sum E_i A_i/l_{0i} - \sum E_i A_i \alpha_i (\Theta_i - \Theta_{0i}), \tag{5-51}$$

where x = path coordinate along the substrate surface, m = mass of individual elements i, E = Young's modulus, A = cross-sectional area of individual elements i, α = temperature-dependent coefficient of thermal expansion, Θ_i = instantaneous temperature of individual elements i, l_{0i} = length of element in the unstressed state, and Θ_{0i} = maximum temperature of the $(i-1)$st coating lamella. Equation (5-51) is a special form of the fundamental Newton momentum equation. Each particle arriving at the surface is incorporated at the precise moment when the supporting $(i-1)$st lamella has reached its maximum temperature Θ_{0i}. Therefore the total lateral ex-

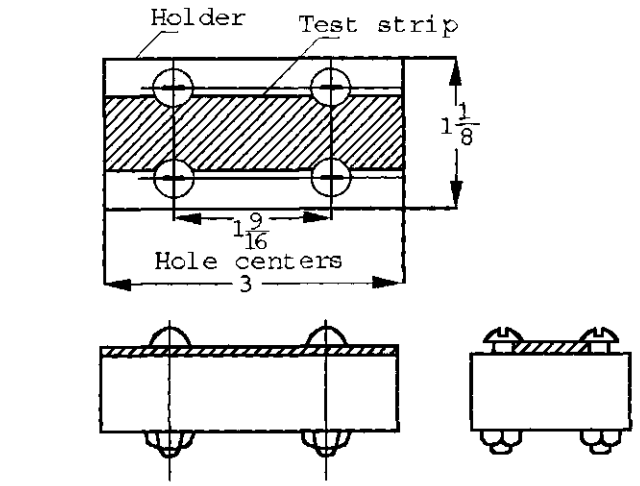

(a)

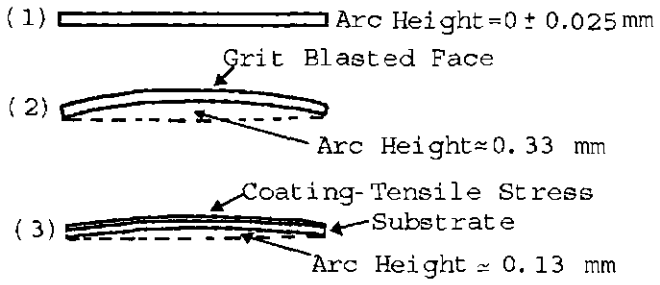

(b)

Figure 5-21. ALMEN test configuration, (a) mounting block, (b) a thin foil before (1) and after grit blasting (2). The convex curvature will be reduced by tensile stresses induced during coating (3). After [83].

pansion can be calculated from the instantaneous thermal expansion and the size of the substrate prior to deposition.

In the second state, after termination of the deposition process the length of the individual elements can be calculated by

$$l_i = l_{0i}[1 + \alpha_i(\Theta_i)(\Theta_i - \Theta_{0i})], \tag{5-52}$$

where l_i is the length that an element would attain at the temperature Θ if it could

adjust freely, i.e. unconstrained by the surrounding elements. The internal strain among individual elements can be calculated considering the bending moments and applying equations developed for bimetallic strips [86].

Verification of the model was done using experimental data obtained by depositing alumina (100 μm thick coatings) and stabilized zirconia (40 μm thick coatings) on ferritic and austenitic steel substrates. Internal strains were measured by the blind hole method (see Sec. 5.5.5.1). Even though the measured internal strain values were found to be lower than the calculated ones due to variations introduced by the drilling process, there is good agreement between the qualitative trend of the measured and the calculated internal strains.

Theoretical work has been performed at UKAEA's Harwell laboratory by Eckold *et al.* [87] on plasma-sprayed stabilized zirconia coatings deposited onto 304 stainless steel. The model considers transfer of heat to the substrate from the molten impinging particles as well as redistribution of heat radiatively and/or convectively to the surrounding atmosphere. The heat transfer model applied uses a number of constraints such as:

- continuity of the coating process,
- coating area is large compared to its thickness,
- heat loss can be described by standard convection and radiation heat loss equations,
- start of spraying approximates to a coating of infinitesimal thickness, and
- thermophysical and elastic properties are temperature-invariant.

The heat transfer model generates data that predict the thermal history of a coating during deposition. From this data the stress history of the coating is being calculated that aids in the prediction of the final residual stress state in the coating. Sensitivity analyses consider the influence of the following parameters on the stress state:

- deposition rate,
- plasma temperature (enthalpy),
- substrate temperature,
- final coating thickness,
- coating area,
- substrate area,
- thermal conductivity, specific heat and latent heat of coating,
- density, emissivity, Poisson ratio, Young's modulus and expansivity of the coating, and
- heat capacity and expansivity of the substrate.

The model produces a graphical output of the stress distribution within the coating dependent on a path coordinate x. It indicates that: the stress is everywhere compressive, the stress maximum occurs at the coating's free surface, and the magnitude of the stress (maximum values 25 MPa) is much lower than the operational stress in a diesel engine where such thermal barrier coatings (TBC) may be applied. As a first approximation it appears that the residual stresses ocurring in such zirconia coatings

are not at all life limiting. However, because of the rather low Weibull modulus of ceramic coatings in general, failure probability is high. In particular, coating fracture stresses in ceramic coatings can be of the same order of magnitude as the residual stresses predicted by this model.

As pointed out by Steffens *et al.* [88] rather large errors will be introduced into thermal and residual stress calculations by neglecting the temperature dependence of the modulus of elasticity. Furthermore, since thermal barrier coatings are designed to be highly porous to minimize their thermal diffusivity, the strong dependence of the modulus on porosity must be considered. In the stress calculations performed [88] to determine the influence of residual and thermal stresses on the thermal shock resistance of yttria-stabilized zirconia TBCs, the following equation was used:

$$\sigma = [Ec(\alpha s - \alpha c)\Delta T]/(1 - vc), \tag{5-53}$$

where the subscripts c and s refer to coating and substrate, respectively. This simplified equation does not consider the substrate rigidity E_s, Poisson ratio of the substrate and the coating thickness as done in the more comprehensive Dietzel equation discussed above (Eq. (5-46)). Since the residual stresses can be somewhat controlled by substrate preheating the normally occuring stress relaxation by micro- or even macrocracking of TBCs can be suppressed. Furthermore, the steep stress gradients at the interface coating/substrate where the stress state changes from tensile to compressive can be smoothed by inserting a soft compliant intermediate bond coat layer or a graded metal–ceramic coating [89].

References

[1] D. Apelian in *Mat. Res. Soc. Symp. Proc.* (Eds. J. Szekely, D. Apelian) **1984**, Vol. 30.
[2] J. Madjeski, *Int. J. Heat Mass Trans.* **1976**, *19*, 1009.
[3] R. McPherson, *J. Mat. Sci.* **1980**, *15*, 3141.
[4] J. M. Houben, *Proc. 2nd NTSC*, 31 Oct–2 Nov **1984**. Long Beach, CA, USA.
[5] H. Gruner, *Thin Solid Films*, **1984**, *118*, 409.
[6] H. Herman, *Sci. Am.* **1988**, 112.
[7] J. M. Houben, Relation of the adhesion of plasma sprayed coatings to the process parameters size, velocity and heat content of the sprayparticles. Ph.D.Thesis, Technical University Eindhoven, The Netherlands, **1988**.
[8] G. Trapaga, J. Szekely, *Metall. Trans. B* **1991**, *22*, 901; R. McPherson, *Surf. Coat. Technol.* **1989**, *39/40*, 173.
[9] S. Fantassi, M. Vardelle, A. Vardelle, M. F. Eichinger, P. Fauchais, *Proc. TS'93*, Aachen **1993**, DVS, Oberursel 152, 387.
[10] A. Hasui, S. Kitahara, T. Fukushima, *Trans. Nat. Jpn. Res. Inst. Met.* **1970**, *12*(1), 9.
[11] H. Maruo, Y. Hirata, Y. Matsumoto, *Proc. 14th ITSC'95 Kobe* 22–26 May **1995**, 341.
[12] M. Fukumoto, S. Kato, I. Okane, *Proc. 14th ITSC'95, Kobe* 22–26 May, **1995**, 353.
[13] O. P. Solonenko, A. Ohmori, S. Matsuno, A. V. Smirnov, *Proc. 14th ITSC'95 Kobe* 22–26 May, **1995**, 359.
[14] H. Harlow, J. E. Welch, *Phys. Fluid.* **1965**, *8*, 12.
[15] H. Jones, *J. Phys. D: Appl. Phys.* **1971**, *4*, 1657.

[16] L. Pawlowski, *The Science and Engineering of Thermal Spray Coatings*, Wiley, New York, USA, **1995**.
[17] H. Kreye, D. Fandrich, H. H. Müller, G. Reiners, in *Advances in Thermal Spraying*, (Ed. N. F. Eaton) (Proc. 11th ITSC, Montreal, 8–12 Sept.) 1986, Welding Inst. of Canada, **1986**, p. 121.
[18] M. H. Rice, R. G. McQueen, J. M. Walsh, in *Solid State Physics, VI* (Eds. F. Seitz and D. Turnbull), Academic Press, New York, USA, **1958**.
[19] R. B. Heimann, *Proc. Adv. Mater.* **1991**, *1*, 181.
[20] S. Kitahara, A. Hasui, *J. Vac. Sci. Technol.* **1974**, *11*, 747.
[21] C. F. Chyba, P. J. Thomas, K. J. Zahnle, *Nature* **1993**, *361*, 40.
[22] H. G. Zachmann, *Mathematik für Chemiker, 4.Auflage*, VCH, Weinheim **1991**.
[23] R. B. Heimann, T. A. Vu, M. L. Wayman, *Eur. J. Mineral*, submitted.
[24] M. Bertagnolli, M. Marchese, G. Jacucci, *J. Thermal Spray Technol.* **1995**, *4*(1), 41.
[25] H. Kühn, O. Stitz, R. Letzner, *Proc. Thermal Spray Conf., TS 90* (DTV 130) Essen, 29–31, August, **1990**, p. 38.
[26] B. B. Mandelbrot, *The Fractal Geometry of Nature*, Freeman, San Francisco, USA, **1982**.
[27] D. W. Schaefer, *Science* **1989**, *243*, 1023.
[28] D. Avnir, D. Farin, P. Pfeifer, *J. Coll. Interface Sci.* **1985**, *103*(1), 112.
[29] E. E. Underwood, K. Banerji, *Mater. Sci. Eng.* **1986**, *80*, 1.
[30] D. Stoyan, H. Stoyan, *Fractals, Random Shapes and Point Fields. Methods of Geometrical Statistics.* Wiley, New York, USA, **1995**; D. Stoyan, H. Stoyan, *Fraktale, Formen, Punktfelder. Methoden der Geometrie-Statistik*, Akademie Verlag GmbH, Berlin, **1992**.
[31] P. Meakin, *J. Mater. Educ.* **1989**, *11*, 105.
[32] B. B. Mandelbrot, *Physica Scripta*, **1985**, *32*, 257.
[33] M. Kardar, G. Parisi, Y.-C.Zhang, *Phys. Rev. Lett.* **1986**, *56*, 889.
[34] S. Amada, T. Hirose, K. Tomoyasu, *Proc. 14th ITSC'95*, Kobe, 22–26 May, **1995**, 885.
[35] Y. Fahmy, J. C. Russ, C. C. Koch, *J. Mater. Res.* **1991**, *6*(9), 1856.
[36] J. J. Mecholsky, D. E. Passoja, K. S. Feinberg-Ringel, *J. Am. Ceram. Soc.* **1989**, *72*(1), 60.
[37] J. E. Yehoda, R. Messier, *Appl. Surf. Sci.* **1985**, *22/23*, 590.
[38] R. F. Voss, R. B. Laibowitz, E. I. Alessandrini, In, *Scaling Phenomena in Disordered Solids* (Eds. R. Pynn, A. Skjeltorp), Plenum Press, New York, **1985**, 279.
[39] J. L. LaRosa, J. D. Cawley, *J. Am. Ceram. Soc.* **1992**, *75*(7), 1981.
[40] B. B. Mandelbrot, D. E. Passoja, A. J. Paullay, *Nature* **1984**, *308*, 721.
[41] D. E. Passoja, D. J. Amborski, *Microstruct. Sci.* **1978**, *6*, 143.
[42] M. Inada, T. Maeda, T. Shikata, *Proc. ATTAC'88, Adv. Thermal Spraying Technology and Allied Coatings*, Osaka, May **1988**, p. 211.
[43] A. S. Khanna, A. K. Patniak, K. Wissenbach, *Proc. 14th ITSC'95*, Kobe, 22–26 May, **1995**, p. 993.
[44] N. Takasaki, M. Kumagawa, K. Yairo, A. Ohmori, *Proc. 14th ITSC'95*, Kobe, 22–26 May, **1995**, p. 987.
[45] R. B. Heimann, D. Lamy, V. E. Merchant, *Trans. 17th Workshop CUICAC* (Ed. R. B. Heimann), Québec City, Québec, Canada, 2 October **1991**.
[46] R. Sivakumar, B. L. Mordike, *Surf. Engineering*, **1988**, *4*, 127.
[47] I. Zaplatynsky, The effect of laser glazing on life of ZrO_2 TBSs in cyclic burner tests. NASA Techn. Memorandum 88821, August **1986**.
[48] A. Ohmori, Z. Zhou, K. Inue, K. Murakami, T. Sasaki, *Proc. 14th ITSC'95*, Kobe, 22–26 May, **1995**, p. 549.
[49] K. Moriya, W. Zhao, A. Ohmori, *Proc. 14th ITSC'95*, Kobe, 22–26 May, **1995**, p. 1017.
[50] A. A. Glagolev, *Trans. Inst. Econ. Min. Moscow*, **1933**, 59.
[51] F. Chayes, *J. Geol. USA* **1954**, 62.
[52] G. C. Ulmer, W. J. Smothers, *Am. Ceram. Soc. Bull.* **1967**, *46*, 649.
[53] L. Zagar, *Arch. Eisenhüttenwesen* **1955**, *26*, 561.
[54] A. Dietzel, H. Saalfeld, *Ber. DKG* **1957**, *34*, 363.
[55] H. L. Ritter, L. C. Erich, *Anal. Chem.* **1948**, *26*, 665.
[56] *A Plasma Flame Spray Handbook* (Ed. T. J. Roseberry, F. W. Boulger). Final Report No. MT-043 (March 1977) to Naval Sea Systems Command, Naval Ordnance Station, Louisville, KY, USA, **1977**.

[57] E. W. Washburn, *Proc. Natl. Acad. Sci. USA* **1921**, *7*, 115.
[58] *Evaluation Methods and Equipment for Flame-Sprayed Coatings*, Metco Inc., **1963**, 15 pp. Quoted after [33].
[59] *Plasma Jet Technology*, Technology Survey, NASA SP-5033 (Eds. P. R. Dennis, C. R. Smith, D. W. Gates, J. B. Bond), NASA, Washington, DC, USA, October **1965**, p. 42.
[60] K. Hajmrle, M. Dorfman, *Mod. Dev. Powder Metall.* **1985**, *15/17*, 609.
[61] B. Bouaifi, U. Draugelates, I. Grimberg, K. Soifer, B. Z. Weiss, *Proc. 14th ITSC'95*, Kobe, 22–26 May **1995**, 627.
[62] M. E. Vinajo, F. Kassabji, J. Guyonnet, P. Fauchais, *J. Vac. Sci. Technol.* **1985**, *A3*, 2483.
[63] O. Brandt, *Proc. 14th ITSC'95*, Kobe, 22–26 May **1995**, p. 639.
[64] C. Brunet, S. Dallaire, I. G. Sproule, *Proc. 14th ITSC'95*, Kobe, 22–26 May **1995**, p. 129.
[65] S. Morozumi, M. Kikuchi, S. Kanazawa, *J. Nucl. Mater.* **1981**, *103/104*, 279.
[66] M. Müller, F. Gitzhofer, R. B. Heimann, M. I. Boulos, *Proc. NTSC'95*, Houston, TX, USA, 11–15 Sept. **1995**.
[67] H.-D. Steffens, H.-M. Höhle, E. Ertürk, *Schweissen Schneiden*, **1981**, *33*, 159.
[68] R. Knight, R. W. Smith, *Proc. 5th NTSC* **1993**, Anaheim, CA, USA, p. 607.
[69] J. Drozak, *Haftung und Schichtaufbau von Spritzschichten. Moderne Beschichtungsverfahren.* DGM-Verlag, Düsseldorf **1992**.
[70] H. Salmang, H. Scholze, *Keramik, Teil I*, Springer, Berlin **1982**, p. 237.
[71] S. R. Levine, R. A. Miller, M. A. Gedwill, *Proc. 2nd Conf. on Advanced Mat. for Alternative Fuel-Capable Heat Engines*, Monterey, CA, USA, **1981**.
[72] J. Mathar, *Arch. Eisenhüttenwesen* **1932**, *6*, 277.
[73] A. Noutomi, *Weld. Int.*, **1989**, *11*, 947.
[74] P. Bialucki, W. Kaczmar, J. Gladysz, *Advances in Thermal Spraying* (Ed. N. F. Eaton), Welding Institute of Canada, Pergamon Press, **1986**, p. 837.
[75] L. C. Cox, *Surf. Coat. Technol.* **1988**, *36*, 807.
[76] B. Eigenmann, B. Scholtes, E. Macherauch, *Mat.-wiss. u. Werkstofftech.* **1989**, *20*, 314.
[77] H.-D. Tietz, B. Mack, L. Pfeiffer, *Proc. TS'93, Aachen* **1993**, DVS 152, p. 205.
[78] C. C. Berndt, *Advances in Thermal Spraying* (Ed. N. F. Eaton), Welding Institute of Canada, Pergamon Press, **1986**, p. 149.
[79] S. Thiele, Mikrohärte, Mikrostruktur und Haftung vakuumplasmagespritzter TiC/Mo_2C/Ni, Co-Verbundschichten. Unpublished diploma thesis. Freiberg University of Mining and Technology, June **1994**.
[80] D. S. Rickerby, *J. Vac. Sci. Technol.* **1986**, *4*, 2809.
[81] W. D. Sproul, *Thin Solid Films* **1984**, *118*, 279.
[82] C. S. Barrett, T. B. Massalski, *Structure of Metals, 3rd edn*, McGraw-Hill: New York, USA, **1966**, p. 465.
[83] *Test Strip, Holder and Gage for Shot Peening*, SAE Standard J 442, SAE Handbook, Part I, SAE Inc., Warrendale, PA, USA **1977**, 9.05–9.06.
[84] P. A. Siemers, W. B. Hillig, *Thermal barrier-coated turbine blade study*, Final report, NASA CR-165351, **1981**, p. 123.
[85] R. Elsing, O. Knotek, U. Balting, *Surf. Coat. Technol.* **1990**, *43/44*, 416.
[86] O. Knotek, R. Elsing, U. Balting, *Surf. Coat. Technol.* **1988**, *36*, 99.
[87] G. Eckold, I. M. Buckley-Golder, K. T. Scott, *Proc. 2nd Conf. Surf. Eng.*, Stratford-on-Avon, UK, 16–18 June **1987**, p. 433.
[88] H.-D.Steffens, Z. Babiak, U. Fischer, *Proc. 2nd Conf. Surf. Eng.*, Stratford-on-Avon, UK, 16–18 June, **1987**, p. 471.
[89] R. Kaczmarek, W. Robert, J. Jurewicz, M. I. Boulos, S. Dallaire, *Proc. Symp. Mater. Res. Soc.* Boston, MA, USA **1983**.